Nanoscale Advances

Accepted Manuscript

This article can be cited before page numbers have been issued, to do this please use: A. B. Siddique, A. Abbas, M. Sher, Y. Zaman, M. F. U. Rehman, U. Nishan and I. Shaaban, *Nanoscale Adv.*, 2026, DOI: 10.1039/D5NA01159K.

ROYAL SOCIETY OF CHEMISTRY

rsc.li/nanoscale-advances

View Article Online
DOI: 10.1039/D5NA01159K

Green synthesis of cubic CuO nanoparticles for biomedical applications and photodegradation of methylene blue: RSM-BBD optimization of reaction parameters, and stability studies

Abu Bakar Siddique,[a,*] Azhar Abbas,[a,b] Muhammad Sher,[a] Yasir Zaman,[c] Muhammad Fayyaz ur Rehman,[a] Umar Nishan,[d] Ibrahim A. Shaaban [e]

[a] *Institute of Chemistry, University of Sargodha, Sargodha 40100, Pakistan*

[b] *Department of Chemistry, Government Ambala Muslim College, Sargodha 40100, Pakistan*

[c] *Department of Physics, University of Sargodha, Sargodha 40100, Pakistan*

[d] *Department of Chemistry, Kohat University of Science and Technology, Kohat 26000 KP, Pakistan*

[e] *Department of Chemistry, Faculty of Science, Research Center for Advanced Materials Science (RCAMS), King Khalid University, P.O. Box 960, Abha, 61421, Saudi Arab*

* *Corresponding authors*: abubakar.siddique@uos.edu.pk

View Article Online
DOI: 10.1039/D5NA01159K

Abstract

Aquatic pollution poses an immense risk to human health and environmental preservation, with azo dyes from textile wastewater being a major source. Nanotechnology offers excellent methods for wastewater treatment, particularly through sunlight-driven photocatalysis. In this study, copper oxide nanoparticles (CMFE@CuO NPs) were produced by an ecofriendly green approach using *C. macrocarpa* fruit extract. The produced NPs were completely examined using advanced analytical techniques, indicating a crystallite size of 16.9 nm and high stability. CMFE@CuO NPs displayed outstanding photocatalytic performance for methylene blue degradation under sunshine. Reaction conditions were tuned using response surface approach based on a Box-Behnken design. Under optimal parameters (50 mg catalyst, 10 ppm dye, pH 8, and temperature of 358 K), 99.9% dye degradation was accomplished within 120 minutes, with a rate constant of 4.44×10^{-2} min^{-1}. Total organic carbon analysis demonstrated 81% mineralization within 4 hours, while regeneration experiments confirmed significant reusability with only a 7% activity decrease after five cycles. Radical scavenging investigations supported the postulated degradation mechanism. In addition to photocatalytic activity, CMFE@CuO NPs demonstrated considerable biological performance, demonstrating strong antibacterial efficacy and high antioxidant activity, comparable to gallic acid. Overall, the findings indicate CMFE@CuO NPs as a very effective, reusable, and versatile nanocatalyst for the treatment of wastewater and environmental remediation.

Keywords: Copper oxide nanoparticles; Response surface methodology; Photodegradation of MB; *Carissa macrocarpa* fruit extract; Photocatalyst; Biological Applications

1. Introduction

View Article Online
DOI: 10.1039/D5NA01159K

Our environment has suffered an immense transformation in recent years due to advances in industry. The industrial effluents are the cause of environmental pollution, and these poisonous wastes are continuously poisoning the water bodies [1]. Water bodies are contaminated by a variety of organic and inorganic pollutants, heavy metals, and endocrine-disrupting chemicals discharged from food, pharmaceutical, leather, textile, and cosmetic facilities. Among these pollutants, azo dyes exhibit the most radical effects in disrupting the aquatic ecosystem [2]. Over 70% of the 900,000 metric tons of dyes produced each year are azo dyes [3]. These dyes present in the effluents are directly mixed with the freshwater reservoirs, resulting in the disruption of the photosynthetic activity of aquatic plants by limiting the sunlight and oxygen demand [4]. Among various hazardous dyes, methylene blue (MB), a cationic azo dye, is known to cause numerous ailments, including skin and eye irritation, gastric disorders, respiratory issues, and even cancer. MB is also reported to cause hypertension, precordial pain, fever, headache, and bladder irritation [5]. Therefore, the mitigation or complete removal of these pollutants is necessary for a balanced aquatic ecosystem and ultimately for human health [6, 7]. MB is a popular model dye in photodegradation studies due to its vivid coloration, distinct UV-visible spectral peaks, extensive use in the textile industry, and accessibility, making it a relevant subject for wastewater treatment research [8].

Among many methods, such as adsorption, chemical oxidation, precipitation, and photocatalytic degradation, opted for organic pollutants removal, the photodegradation is considered as the most viable, economic, and environmentally benign approach [9]. Photodegradation on nanomaterials requires no hazardous chemicals or high energy requirements and results in the complete oxidation of azo dyes to carbon dioxide and water. Upon exposure to suitable light wavelengths, metal-based nanoparticles (NPs) are activated to generate electron-hole (e-/h+) pairs, actively involved in production of reactive oxygen species (ROS). These ROS can easily destruct the covalent bonds

View Article Online
DOI: 10.1039/D5NA01159K

of azo dyes by redox reactions and convert them into less or non-hazardous species [10]. Many metal-based NPs have been tried previously for photodegradation potential, but these materials are still interested in completely mineralizing azo dyes in the shortest time [10, 11]. In this regard, greenly synthesized NPs are highly opted due to their easy generation, non-hazardous nature, large surface area, and efficient sunlight response to degrade pollutants.

Sunlight-responsive copper oxide NPs (CuO NPs) are an important material that can effectively degrade organic pollutants under sunlight within a short time. Due to a large volume-to-surface area ratio, sunlight-responsive bandgap, high stability at high temperature, and cost-effective raw materials, CuO NPs are believed to be an important candidate as a photocatalyst [12]. The optical and catalytic properties of CuO NPs can further be improved by surface functionalization with bioactives that can easily adsorb dye molecules on their surface [13]. Several previous studies have shown high catalytic and biological efficacy of greenly synthesized CuO NPs, such as Atri *et al*., reported the *Ephedra Alata* extract-assisted biosynthesis of CuO NPs for photodegradation of MB [14] and Koteeswari *et al.,* documented the photodegradation of MB using papaya and banana peel mediated synthesized CuO NPs [12]. Additionally, in recent years, many CuO- based nanocomposites have also attracted significant attraction owing to their multifaceted applications in field of catalysis and biological applications. For instance, Arulkumar *et al*., reported the CuO@Fe_2O_3 nanocomposites to degrade crystal violet dye (92.82%) and antimicroboial applications to hinder the growth of *S. aureus*, *E. coli* and *C. albicans* [15]. However, the quest for the synthesis of surface-modified and eco-friendly CuO NPs by green synthesis to completely degrade the azo dyes by facile generation of ROS is still ongoing.

Recently, plenty of plant-based materials have been exploited for the eco-friendly synthesis of NPs, but the exploration of fruit extract that are not widely used as food is an interesting area. Due

View Article Online
DOI: 10.1039/D5NA01159K

to enriched phytochemicals, the fruit extracts act as a better bio-based reducing agents along with the additional advantages of natural, renewable origin, rich phytochemical composition, and non-toxic nature, making them environmentally friendly and sustainable as compared to chemical methods of NPs synthesis which use toxic solvents or chemicals. [16, 17] Although the reduction efficiency of fruit extracts may vary depending on the nature, method of extraction and phytochemical composition, still the use of these extracts gives better or at least comparable reduction efficiency as compared to other alternatives, like microbial extracts or leave extracts. [16, 18, 19] In this regard, one of the phytochemically enriched fruits is the *C. macrocarpa* fruit, known as the natal plum. This fruit is a rich source of several antioxidants, vitamins, flavonoids, and phenolics [20, 21]. The aqueous extract of this fruit has been reported to synthesize many stable metal based NPs, like AgNPs, [22] AuNPs, [23] CdO NPs, [24] NiO NPs, [25] and ZnO-NiO NCs [26] but has never been explored to synthesize CuO NPs. Due to no previous work reported to synthesize CuO NPs by *C. macrocarpa*, this research work might prove an essential addition to existing literature in cost-effective photodegradation studies of azo dyes and biomedical applications.

A number of reaction variables, i.e., pH of dye solution, temperature, and dye concentration, also play important roles in the degradation efficiency of the catalyst. The high efficiency of degradation by the catalyst can be obtained by the optimization of the reaction conditions. A combination of experimental work and statistical calculations by machine learning tools is an advanced method to optimize the reaction parameters. The response surface methodology (RSM) based optimization of reaction parameters has been extensively studied currently [27]. Therefore, this method has been selected for optimization of photodegradation reaction, as evidenced by previously reported work [28]. By optimization of parameters, the high catalytic efficiency can be obtained, which is necessary for the commercial applications.

View Article Online
DOI: 10.1039/D5NA01159K

In addition to the catalytic applications, the nanotechnology has also served the humanity to tackle various biomedical issues, ranging from eradication of microbial pollution and sensing of antibiotics to the tissue generation and cancer therapy [29-33]. Among several water pollution issues, microbial water pollution is also an imminent threat to the freshwater reservoirs [34]. The exceptional antimicrobial and anti-oxidative properties of plant extracts further emphasize the potential of bio-fabricated NPs as potent antibacterial materials and antioxidants [35]. These NPs can hinder the normal functioning of bacterial cells by easily crossing the membrane barriers due to their small size and phytochemically enriched surface. On entering the bacterial cells, they interact with cellular organelles and the genome either directly or by producing ROS, causing various cell mutations that ultimately lead to bacterial death. Moreover, due to the high reducing properties of CuO NPs and the Phyto-functionalized surface, the greenly synthesized NPs may also reduce the oxidizing species produced as a result of various metabolic reactions. Therefore, these NPs can also have applications in creams, ointments, and surface cleanings [36].

The current work presents *C. macrocarpa* aqueous extract-based green synthesis of CuO NPs. The reported CuO NPs have been thoroughly characterized by UV-visible and FTIR spectroscopy, PXRD, DLS and Zeta potential, SEM, EDX, TGA, and TEM. The post characterized, Phyto-functionalized CuO NPs were assessed for photocatalytic disintegration of MB dye under intense sunlight, and the RSM-BBD model was adopted to optimize reaction conditions. Afterward, the antibacterial and antioxidant potential of the CuO NPs were also assessed for biological applications.

2. Experimental Work

2.1. Chemicals and Instruments Used

View Article Online
DOI: 10.1039/D5NA01159K

AR-grade chemicals were procured from reliable suppliers Sigma Aldrich and Merck (Germany) to perform experiments. Ultra-pura deionized water was utilized as aqueous medium for preparation and dilution of all the necessary solutions. Throughout the experimental work, the glassware was carefully cleaned with chromic acid, rinsed with distilled water and dried in hot-air oven to ensure sterility. Fresh fruits of *C. macrocarpa* (Figure S1) were obtained from the botanical sanctuary of University of Sargodha, Pakistan.

The PXRD spectrum was obtained using the JDX-3532 diffractometer from JEOL, Japan, utilizing Cu-Kα radiation (λ = 1.5418 Å) in the 2θ range of 10–80°. FTIR analysis was conducted using an FTIR spectrophotometer (Shimadzu FTIR-8400S, Japan). While a UV-vis spectrophotometer (Shimadzu pharmaspec-1700, Japan) was used to record the optical absorption spectra. Morphological analysis of samples was performed utilizing SEM with the JSM5910 equipment and TEM with the JEM-ARM2000F instrument, JEOL, Japan.

2.2. Preparation of *C. macrocarpa* fruit Extract

The preparation of CMFE was carried out according to methodology outlined in the literature [21, 37]. The initial steps involved in the aqueous extraction of *C. macrocarpa* fruits included washing of fruit with DW to remove surface contamination, shade-drying at room temperature, chopping to separate seeds from fruit pulp, and grinding of dried pulp to obtain a homogeneous powder. Subsequently, an accurately weighed amount (~10 g) of the dried fruit powder was added to 100 mL of deionized water in a 250 mL round bottom flask. The resulting solution was subjected to reflux at 90 ºC and left for 3 h while being magnetically stirred at 400 rpm. A deep red-coloured solution was obtained, cooled to room temperature and filtered to separate bioactives-rich liquid extract from the solid residues. The clear extract was then evaporated in oven at 80 ºC for 24 h and the subsequent dried powder (CMFE) was stored at 4 ^{0}C for later use in the bio-fabrication of NPs.

View Article Online
DOI: 10.1039/D5NA01159K

2.3. Phytochemical Screening of CMFE

The rich presence of numerous bioactive entities such as phenolics, carbohydrates, tannins, flavonoids, terpenoids, saponins, anthraquinone, and alkaloids in CMFE was verified through a series of distinctive qualitative assays namely, Lead Acetate Test, Molisch Test, Braymer's Test, Shinoda Test, Salkowski Test, Foam Test, Borntrager Test, and Draggendorff Test, respectively [21, 38, 39].

2.4. Biogenic preparation of CuO NPs

A typical green synthesis approach was employed to prepare CMFE@CuO NPs. To do this, a 20 mg/15 mL of CMFE extract was added dropwise to 20 mL of 30 mM $Cu(NO_3)_2 \cdot 2H_2O$ solution under constant reflux conditions at 100 ºC with a stirring rate of 200 rpm. To the above solution, a 0.1 M solution of NaOH was introduced dropwise to adjust its pH at 9, providing an alkaline medium for production of stable NPs with controlled size and defined morphology. On appearance of brown precipitates in the mixture, the reaction was stopped and the solution cooled to room temperature. The obtained suspension was centrifuged at 8000 rpm to isolate the precipitates which were then washed thrice with deionized water to remove the soluble salts and unused extract. The purified precipitates were then dried in oven at 150 ºC for 2 h and calcined in a muffle furnace at 400 ºC for 3 h yielding a uniform powder of CMFE@CuO NPs for further analysis.

2.5. Photocatalytic activity evaluation of CMFE@CuO NPs

The photocatalytic performance of freshly synthesized CMFE@CuO NPs was evaluated through the sunlight-driven degradation of methylene blue (MB) following a standard procedure [40]. Briefly, 10 mg of CMFE@CuO NPs were dispersed in 20 mL of 10 ppm MB solution and magnetically stirred in the dark at 200 rpm for 20 minutes to establish adsorption-desorption equilibrium. The

View Article Online
DOI: 10.1039/D5NA01159K

reaction mixture was then exposed to direct sunlight for 2 hours in June (15-25 June, 2025), between 10:00 am and 02:00 pm at the University of Sargodha with an average light intensity of 900 W/m². After every 15-minutes, aliquots were taken and absorbance was measured to monitor the gradual decrease in MB absorbance at 668 nm. The photocatalytic degradation efficacy (%) was calculated using the absorbance data (**Equation 1**), enabling quantitative assessment of the catalyst's performance [41, 42].

$$\text{Degradation of MB Dye (\%)} = \frac{C_0 - C_f}{C_0} \times 100 = \frac{A_0 - A_f}{A_0} \times 100 \quad (1)$$

C_0 and C_f denote the starting and final concentrations of the dye, respectively. **Figure S2** illustrates the overall framework of photocatalytic activity investigations. Based on the comprehensive literature review, the impact of various reaction parameters, such as pH (3-13), catalyst dosage (10-50 mg), initial dye concentration (10-30 ppm), and temperature (298-358 K), on degrading efficiency was also recorded [23, 43, 44]. The statistical tool, i.e., RSM/BBD was employed to optimize these variables of reaction.

2.6. Experimental Design of RSM/BBD

RSM encompasses statistical and mathematical approaches employed to assess the interrelationships among various process variables affecting pollutant degradation [28, 45]. This work utilized the Box-Behnken design (BBD) to systematically optimize the experimental settings. Each variable was analyzed at two coded levels: low (-1) and high (+1), as detailed in **Table S1**. A total of 29 experimental runs were performed to analyze methylene blue deterioration across the four specified parameters. The experimental results were later compared with model-predicted values to validate the reliability and appropriateness of the BBD model.

2.7. Total Organic Content (TOC) Analysis

View Article Online
DOI: 10.1039/D5NA01159K

The fading of the dye solution's color does not reflect the complete mineralization of dye molecules. The partial breakdown of dyes can lead to the creation of numerous harmful chemicals in water , which further impair the water quality [42]. Dissociation of diazenyl group induce substantial discoloration of dye solution [46]. Therefore, evaluating total organic content (TOC) value is vital to verify the complete mineralization of dyes. TOC removal percentage was calculated using the **Equation 2** given below [47].

$$\%\text{Removal of TOC (Mineralization)} = \frac{(TOC_0 - TOC_t)}{TOC_0} \times 100 \qquad (2)$$

where, TOC_o is the initial concentration of organic content while TOC_t is the concentration of organic content after time 't'.

2.8. Reusability Studies of Catalyst

To check the activity of the catalyst for repeated usage, the reusability experiments were executed on the surface of CMFE@CuO NPs for five consecutive cycles. After each usage, CuO NPs were recovered using an already documented procedure [48]. Soon after MB degradation, the catalyst was recovered by centrifugation of resulting mixture for 30 min, rinsed with distilled water and reactivated via 3 hours of oven-drying. Afterward, the recovered catalyst was successfully employed for the next photocatalytic batch experiment.

2.9. Disc Diffusion Assay

The antibacterial activity of CMFE and CMFE@CuO NPs was evaluated using the standard disc diffusion assay, following previously reported methods [21, 49]. Two Gram-negative bacteria (*Escherichia coli* and *Pseudomonas aeruginosa*) and two Gram-positive bacteria (*Staphylococcus aureus* and *Bacillus subtilis*) were selected to assess the bactericidal efficacy of the materials.

View Article Online
DOI: 10.1039/D5NA01159K

Bacterial cultures were grown in nutrient agar (2.5 g/100 mL), and the cell density was adjusted to approximately 10^8 CFU/mL with saline. Fresh agar medium (92.5 g/100 mL) was prepared, poured into Petri dishes, sterilized, and inoculated with the respective bacterial strains. After solidifying, sterile paper discs saturated with CMFE (2 mg/5 mL) and CMFE@CuO NPs (2 mg/5 mL) were placed onto the agar surface. The plates were then left incubated at 37 °C for 24 hours. Antibacterial activity was assessed by measuring the diameter of the inhibition zones created around each disc, and the results were analyzed to evaluate the relative efficacy of the materials against the tested bacterial strains.

The MIC values of CMFE and CMFE@CuO NPs were also determined by the broth microdilution method for accurate quantification of antibacterial activity. For this purpose, a series of aqueous dilutions of CMFE and CMFE@CuO NPs were prepared in the range of 50-500 µg/mL, and fresh bacterial cultures of *E. coli, P. aeruginosa, S. aureus,* and *B. subtilis* were inoculated in nutrient broth and incubate at 37 °C overnight. After adding the CMFE and CMFE@CuO NPs dilutions to the bacterial inoculum, and overnight incubation at 37 °C. The MIC value against each bacterial strain was calculated and reported in µg/mL.

2.10. DPPH assay

The antioxidant efficacy of samples was tested using the frequently used DPPH radical scavenging assay, which is based on hydrogen atom transfer processes [50]. A 0.1 mM DPPH solution (3.9 mg in 100 mL methanol) was produced and stored in the dark for 2 hours. A blank was made by combining 1.2 mL of DPPH solution with 800 µL of methanol, exhibiting a high absorbance at 517 nm. Methanolic solutions of CMFE, CMFE@CuO NPs, and gallic acid (standard) were prepared at an initial concentration of 1 mg/mL and serially diluted to obtain concentrations ranging from 12.5 to 400 µg/mL. For the assay, 800 µL of each test solution was mixed with 1.2

View Article Online
DOI: 10.1039/D5NA01159K

mL of DPPH solution and incubated in the dark for 30 minutes. A visible color change from deep violet to pale yellow upon nanoparticle addition indicated effective radical scavenging. Following incubation, absorbance was measured at 517 nm, and the percentage radical scavenging activity and IC_{50} values were calculated using standard equations (**Equations 3 and 4**).

$$\text{DPPH Radical Scavenging Activity}\,(\%) = \frac{(A_0 - A_s)}{A_0} \times 100 \quad (3)$$

$$IC_{50} = \frac{(50 - \text{intercept})}{\text{slope}} \times 100 \quad (4)$$

Where, A_0 and A_s shows the absorbance of blank and absorbance of sample solution respectively.

2.11. Statistical Analysis

Triplicate experiments were performed to statistically evaluate results by ANOVA. Accepted results having significance level of p less than 0.05 were reported as mean ± standard deviation.

3. Results and Discussion

3.1. Phytochemical screening of CMFE

Phytochemical analysis indicated the rich presence of various phenolic compounds, terpenoids, saponins, anthraquinones glycosides and sugars in *C. macrocarpa* aqueous extract. The results are illustrated in **Table S2**. The bioactive-rich composition of fruit extract anticipated its potential to reduce the metal NPs because the bioactives especially phenolics play main role in reduction due to presence of abundant -OH groups. Hence, this extract was used for synthesis and capping of CuO NPs.

3.2. UV-Vis and FTIR Analyses

View Article Online
DOI: 10.1039/D5NA01159K

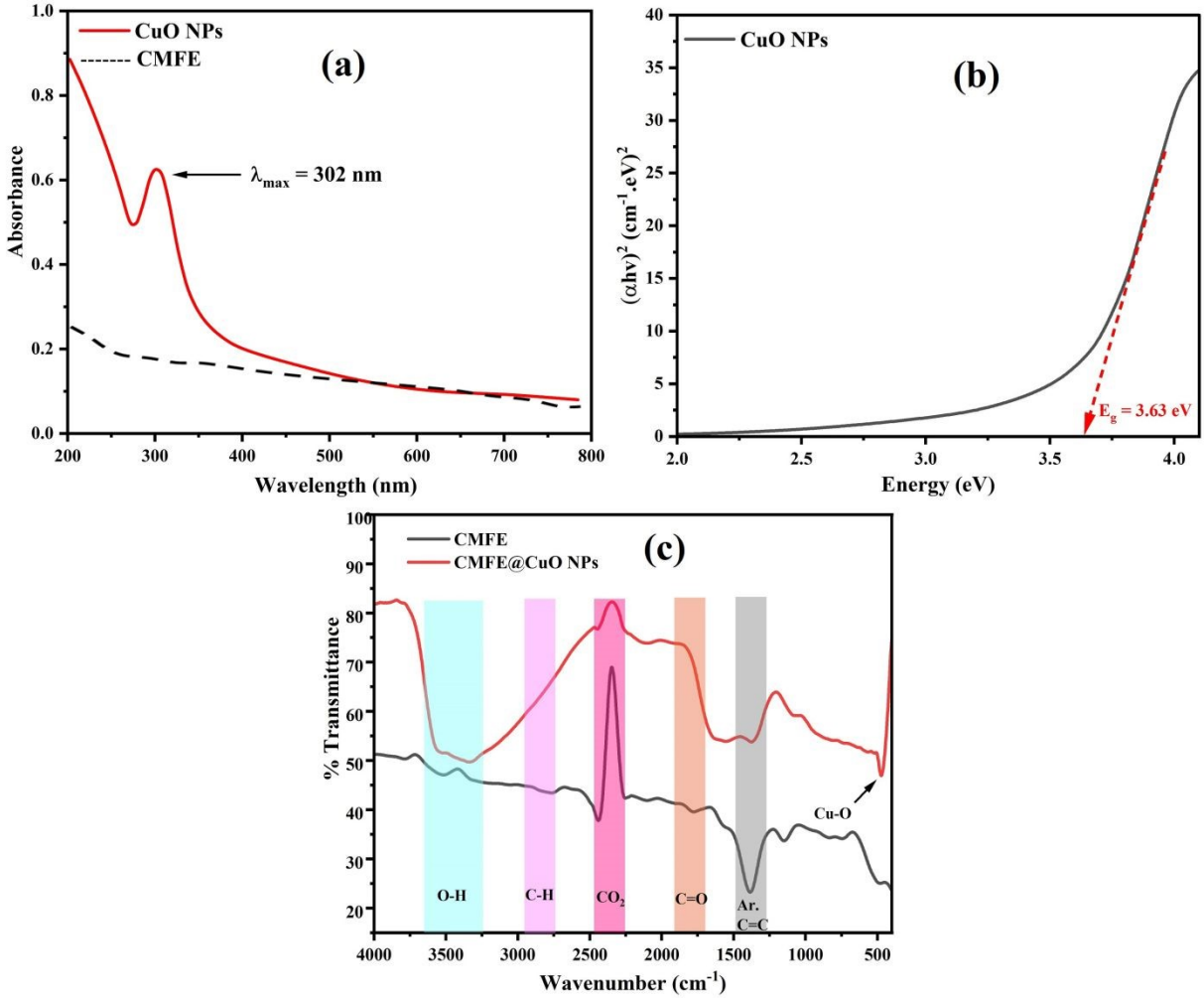

Figure 1. (a) UV–visible absorption spectra of *C. macrocarpa* fruit extract and synthesized CuO NPs, **(b)** Tauc plot used to estimate the optical band gap of CuO NPs, and **(c)** FTIR spectra of CMFE and CMFE@CuO NPs.

The UV-Vis absorption spectra (Fig. 1 (a)) of CMFE@CuO NPs sonicated for 15 min exhibited the typical peak of CuO NPs at 302 nm, but no discernible peak for the CMFE. This distinct peak was attributed to the cumulative oscillations of free electrons at the surface of CuO NPs. In addition, the absorbance data was utilized for constructing the Tauc's plot, which, enabled the bandgap energy to be calculated using **Equation 5** [42].

$$(\alpha h\nu)^{1/n} = B(h\nu - E_g)^n \quad (5)$$

View Article Online
DOI: 10.1039/D5NA01159K

Where 'hν' is photon energy, 'α' is the molar absorption coefficient, 'h' represents Planck's constant while ν and B corresponds to frequency and a constant of proportionality respectively. By plotting the graph, direct energy bandgap (E_g) was found to be 3.63 eV, as shown in figure 1(b). The observed large E_g value reflects the catalyst's ability to respond to sunlight for generation of charge carriers (electron-hole pairs) and was likely due to intragap states in the lattice and quantum confinement effects [51].

The FTIR analysis confirmed the successful coating of NPs with various bioactives through identification of multiple functional groups on the surface of NPs and in the extract. As evidenced by the FTIR spectra (fig.1.(c)) of CMFE and CMFE@CuO NPs, the corresponding functional group peaks were found at 1450 cm^{-1} (C=C stretching) for aromatic compounds, 1690 cm^{-1} (C=O stretching) for carbonyl containing phytochemicals, 2310 cm^{-1} for CO_2, 2940 cm^{-1} (C-H streching) for aliphatic compounds, and 3250-3600 cm^{-1} (O-H stretching) for phenolics and adsorbed moisture [52]. The existence of such peaks demonstrated that the surface of NPs had been well coated. Additionally, a detectable peak around 500 cm^{-1}, indicative of Cu-O stretching, confirmed the metal oxide formation in the crystal lattice.

3.3. PXRD, TEM and EDX analyses

PXRD diffractogram of CuO NPs depicted in **Figure 2a** exhibited typical diffraction peaks at 2θ values of 32.6°, 35.7°, 38.8°, 49.0°, 53.5°, 58.4°, 61.6°, 66.4°, 68.2°, 72.5°, and 75.2°. These strong Bragg's reflections were indexed to (110), (11-1), (111), (20-2), (020), (202), (11-3), (31-1), (220), (311), and (222) lattice planes, confirming the monoclinic phase of CuO NPs in accordance with JCPDS card no. 048-1548. Based on diffraction data, the average crystallite size and other strain parameters, as shown in **Table 1**, were determined by applying the equations given under heading S1 in the supplementary material [53].

View Article Online
DOI: 10.1039/D5NA01159K

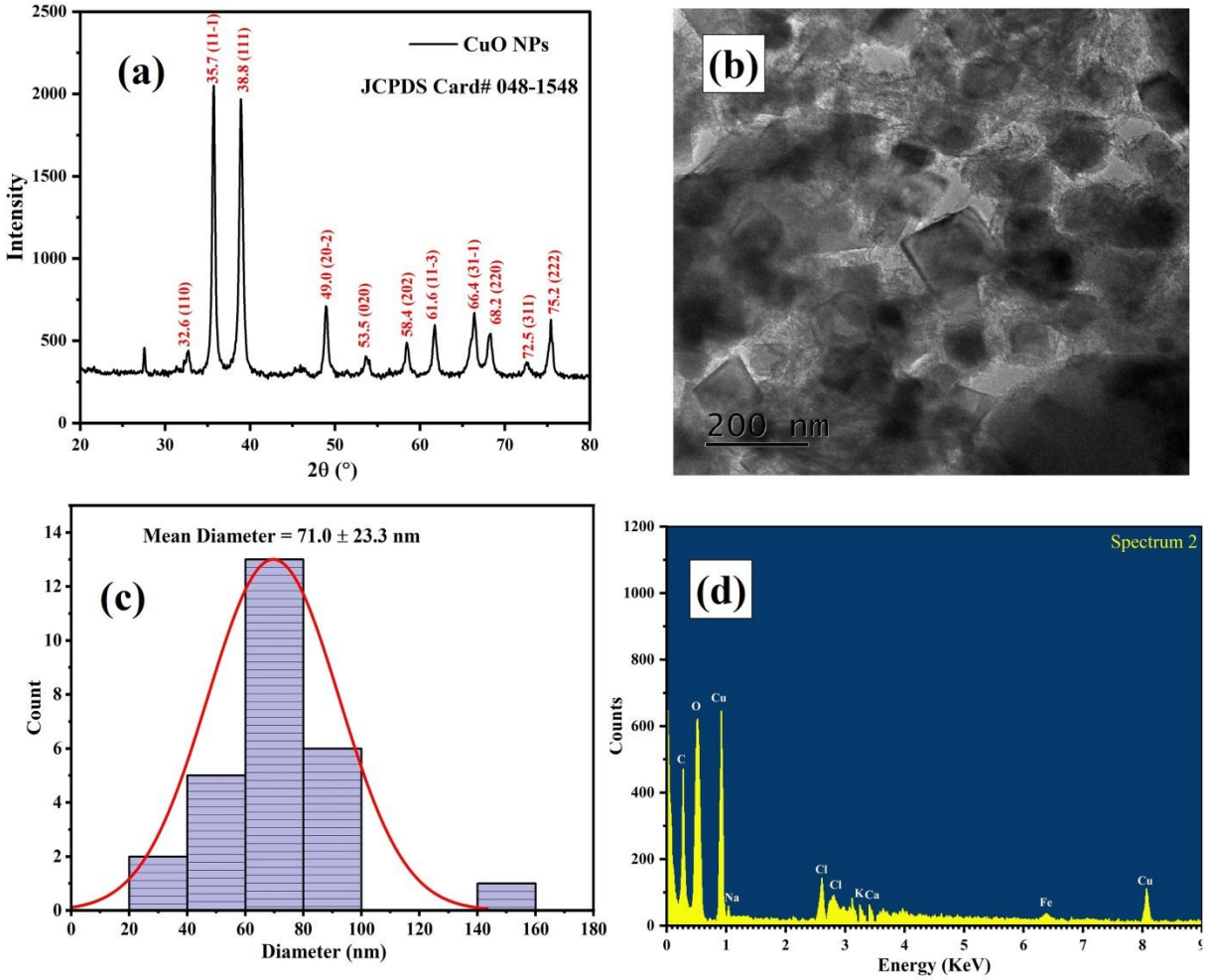

Figure 2. (a) PXRD pattern of green-synthesized CMFE@CuO NPs**, (b)** TEM image illustrating the morphology of CMFE@CuO NPs, **(c)** Particle size distribution histogram of CMFE@CuO NPs, and **(d)** EDX spectrum of CMFE@CuO NPs.

Table 1. Summary of crystallographic lattice parameters of CMFE@CuO NPs

Sample	Average crystallite size 'D' (nm)	Dislocation density $\delta \times 10^{-3}$ (nm^{-2})	Micro strain $\varepsilon \times 10^{-3}$	Degree of Crystallinity (%)
CMFE@CuO NPs	16.9	3.5	0.6	98.9

View Article Online
DOI: 10.1039/D5NA01159K

In addition, scanning electron microscopy (SEM), transmission electron microscopy (TEM), and energy dispersive X-ray spectroscopy (EDX) were used to analyze the CMFE@CuO NPs' morphology and elemental composition, respectively. NPs with size dimensions in the nano range were clearly visible in the scanning electron microscopy image (**Figure S3**). A TEM picture illustrated in **Figure 2b** was recorded to examine the form and particle size of the prepared NPs. Cubic NPs were seen in the TEM picture and the particle size distribution histogram **Figure 2c** revealed an average particle size of 71.0 ± 23.3 nm. The variation in the particle size calculated by TEM images and PXRD analysis was observed, indicating the polycrystalline nature of CMFE@CuO NPs. Based on the PXRD analysis, the calculated crystallite size (16.9 nm) was significantly smaller than the particle dimensions observed in TEM images, suggesting that the cubic structures are composed of multiple crystallites rather than being single-crystal particles. Additionally, the broadened XRD diffraction peaks indicated nanoscale crystalline domains formed by polycrystalline aggregates through oriented growth and agglomeration during synthesis. The EDX spectrum of CMFE@CuO NPs (**Figure 2d**) displayed distinguished peaks of Cu at 0.94 keV and 8.05 keV along with a prominent peak of oxygen at 0.52 keV showing Cu and O as the principal constituents. Some weaker peaks for C, Na, Cl, K, and Fe were also detected, probably stemming from extract derived metabollites or residual contaminants. Typically, these extra peaks are often seen in greenly synthesized NPs [21].

3.4. DLS and ZP analysis of CMFE@CuO NPs

ZP and DLS analyses were used to evaluate the surface charge and hydrodynamic size of CMFE@CuO NPs. The DLS results (**Figure 3a**) showed a particle size distribution ranging from 77 to 98 nm, with an average hydrodynamic diameter of 89.7 ± 4.7 nm. The particle size obtained from TEM analysis was comparatively smaller, which is expected due to the absence of solvent

View Article Online
DOI: 10.1039/D5NA01159K

effects. This difference arises because DLS measurements account for the hydration layer formed around NPs when dispersed in aqueous media, resulting in a larger apparent particle size.

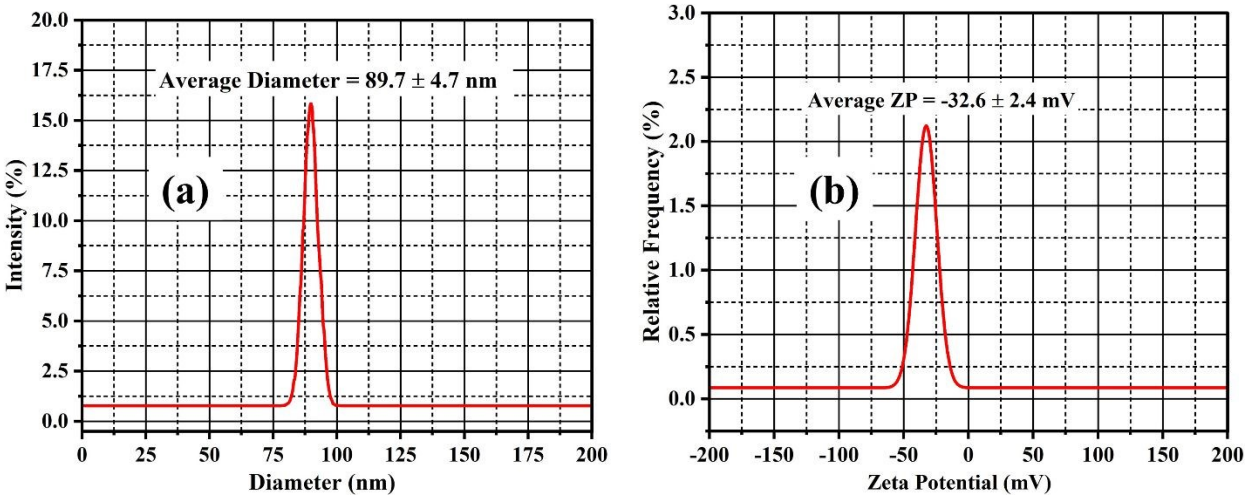

Figure 3. (a) Hydrodynamic radius measurement of CMFE@CuO NPs by DLS analysis, and **(b)** Zeta potential profile of CMFE@CuO NPs.

This magnitude of negative average ZP value of -32.6 ± 2.4 mV (**Figure 3b**) depicted the good stability of CuO NPs on capping with the phytochemicals of CMFE involved in green synthesis of NPs. According to ZP results, the suspension exhibited remarkable electrostatic stability, allowing NPs to remain dispersed for a long time with minimal agglomeration.

3.5. Thermogravimetric analysis of CMFE@CuO NPs

TGA analysis using a thermal analyzer (Discovery 650 SDT, TA Instruments, USA) was conducted to assess the thermal stability of prepared CuO NPs between a temperature range of 25-1000 ºC as shown in **Figure 4**. The findings demonstrated strong concordance with the configuration and decomposition procedure. Thermal degradation occurred in two stages: small weight loss (~1.2%) in 300-1084 K due to water evaporation and moisture loss, and 14.8% weight

View Article Online
DOI: 10.1039/D5NA01159K

loss in 1084-1250 K due to the decomposition of organic moieties. Overall, the sample showed high stability (only 16% weight loss) even at high temperatures.

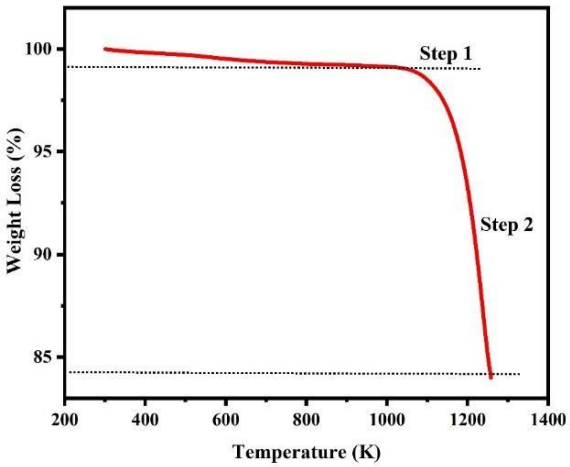

Figure 4. Thermogravimetric plot of CMFE@CuO NPs

3.6. Photodegradation of MB

On the account of having an optimal band gap of 3.63 eV, the prepared CMFE@CuO NPs were investigated for their photocatalytic potential against sunlight-assisted degradation of MB dye. The large E_g value allows the catalyst's valence electrons to absorb sunlight, facilitating their transfer from VB to CB and leading to the formation of excitons (electron-hole pairs). The UV-Vis spectra recorded at regular time intervals indicated a progressive reduction in the dye concentration, as evidenced by a steady decrease in the MB solution's absorption intensity at λmax (668 nm) up to 120 minutes, as illustrated in **Figure S4**.

3.7. RSM/BBD for optimization of MB degradation

The RSM/BBD model was used to observe how four distinct factors and their correlation affected the photodecomposition of MB. **Table 2** displays the findings of the BBD model from 29 experimental trials, including both expected and actual values. These statistics validate the quadratic model's appropriateness for MB degradation. The elevated adjusted R^2 (0.9856) suggests

View Article Online
DOI: 10.1039/D5NA01159K

a robust model fit. While the minimal lack of fit p-value (0.8471), along with a significant sequential p-value (< 0.0001), and the low standard deviation of 2.72, signify model adequacy and good prediction accuracy. **Table S3**. describes the model's fit as proposed by the software, and **Figure S5.** indicates a strong correlation between experimental and anticipated results.

Table 2. Box-Behnken design for optimization of four parameters influencing degradation of MB

Run	A: pH	B: Temperature (K)	C: Concentration of Dye (ppm)	D: Catalyst Dosage (mg)	MB Dye Degradation (%)	
					Actual Value	Predicted Value
1	3	328	30	30	57	60.4
2	13	298	20	30	36.5	37.0
3	8	328	20	30	92.5	90.0
4	13	328	30	30	29	29.3
5	8	298	20	50	88	88.3
6	13	328	20	50	38	37.6
7	8	298	20	10	80.5	79.7
8	8	358	10	30	94	94.2
9	8	328	20	30	92	90
10	13	328	20	10	31	31.7
11	8	328	20	30	90.5	90.0
12	8	328	10	10	84	83.8
13	8	328	30	10	74	74.8

View Article Online
DOI: 10.1039/D5NA01159K

14	3	328	20	50	68	65.7
15	8	358	20	10	75	75.4
16	3	358	20	30	58	58.1
17	3	298	20	30	56	55.3
18	8	328	20	30	84	90.0
19	13	358	20	30	37	38.2
20	3	328	20	10	43	41.8
21	8	298	10	30	91	93.2
22	13	328	10	30	52	49.3
23	8	328	10	50	98	97.7
24	3	328	10	30	56	56.4
25	8	358	20	50	95	96.6
26	8	298	30	30	86	84.2
27	8	358	30	30	91	87.2
28	8	328	20	30	91	90.0
29	8	328	30	50	90	90.7

Moreover, the ANOVA analysis was conducted to validate the importance and relevance of BBD-proposed model and the outcomes are depicted in **Table 3**. The F-value of 138.24 suggests model's significance with 0.01% chance that the noise may have caused this large value.

Table 3. ANOVA of quadratic polynomial model for MB degradation

View Article Online
DOI: 10.1039/D5NA01159K

Source	Sum of Squares	df	Mean Square	F-value	p-value	Remarks
Model	14310.44	14	1022.17	138.24	< 0.0001	significant
A-pH	1092.52	1	1092.52	147.75	< 0.0001	
B-Temperature	12.00	1	12.00	1.62	0.2234	
C-Concentration of Dye	192.00	1	192.00	25.97	0.0002	
D-Catalyst Dosage	667.52	1	667.52	90.27	< 0.0001	
AB	0.5625	1	0.5625	0.0761	0.7867	
AC	144.00	1	144.00	19.47	0.0006	
AD	81.00	1	81.00	10.95	0.0052	
BC	1.0000	1	1.0000	0.1352	0.7186	
BD	39.06	1	39.06	5.28	0.0375	
CD	1.0000	1	1.0000	0.1352	0.7186	
A^2	11340.23	1	11340.23	1533.64	< 0.0001	
B^2	6.49	1	6.49	0.8772	0.3648	
C^2	3.65	1	3.65	0.4934	0.4939	
D^2	100.57	1	100.57	13.60	0.0024	
Residual	103.52	14	7.39			
Lack of Fit	56.02	10	5.60	0.4718	0.8471	not significant
Pure Error	47.50	4	11.88			
Total	14413.97	28				

Model significance was confirmed by P-values below 0.0500, identifying factors A, C, D, their interaction terms (AC, AD, BD), and quadratic terms (A^2 and D^2) as statistically significant contributors to MB degradation. Insignificant terms with P-values greater than 0.1 were excluded from the model to improve predictive accuracy. The lack-of-fit F-value (0.47) was insignificant

View Article Online
DOI: 10.1039/D5NA01159K

relative to the pure error, indicating good model adequacy. A regression equation expressed in coded variables (**Equation 6**) was employed to assess the individual and interactive effects of process parameters on degradation efficiency.

$$MB\ Degradation\,(\%) = 90 - 9.54A + B - 4C + 7.46D - 0.3750AB - 6AC - 4.5AD + 0.5BC + 3.13BD + 0.5CD - 41.81A^2 - B^2 + 0.75C^2 - 3.94D^2 \quad (6)$$

The intercept value of 90 represents the baseline response, while the linear coefficients correspond to the direct effects of the independent variables. Quadratic coefficients account for curvature in the response surface, and interaction coefficients describe the combined influence of paired variables. Model validity was further confirmed through residual diagnostics, including normal probability and residual-versus-run plots (**Figure 5a** and **5b**). The linear distribution of residuals and their random dispersion around the central axis demonstrate the reliability and robustness of the developed model.

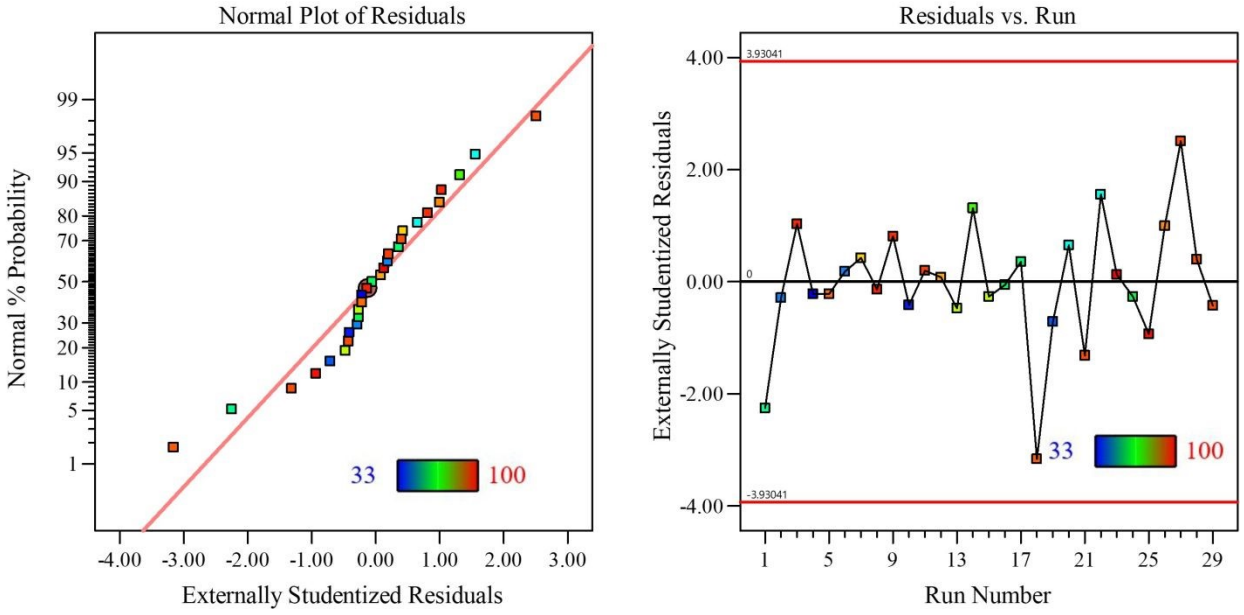

Figure 5. (a) Normal plot of residuals; **(b)** Residual vs run distribution plot

View Article Online
DOI: 10.1039/D5NA01159K

2-D contour plots and 3-D response surface graphs analyze how two factors simultaneously affect dye degradation efficiency across the given ranges by keeping other factors constant. 2-D contour plots and 3-D response surface graphs of various factors are shown in **Figure 6**.

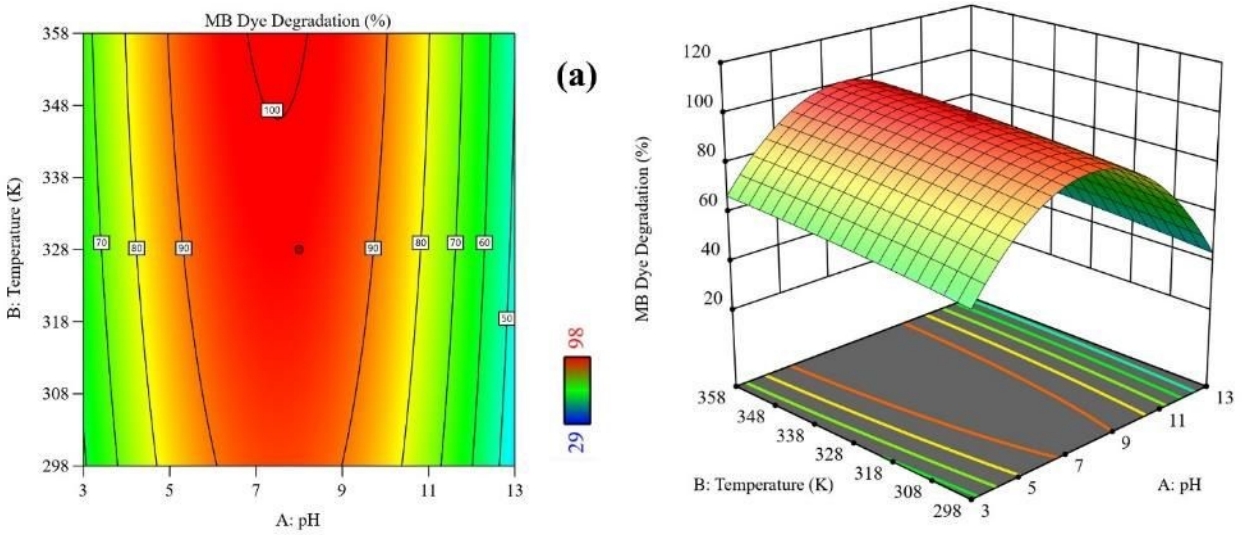

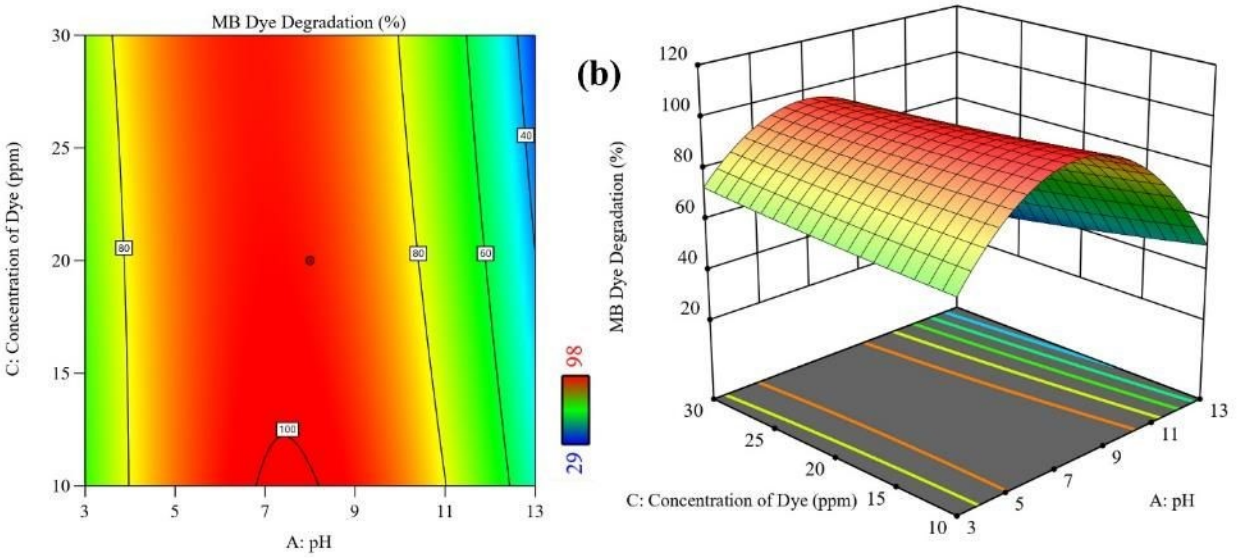

View Article Online
DOI: 10.1039/D5NA01159K

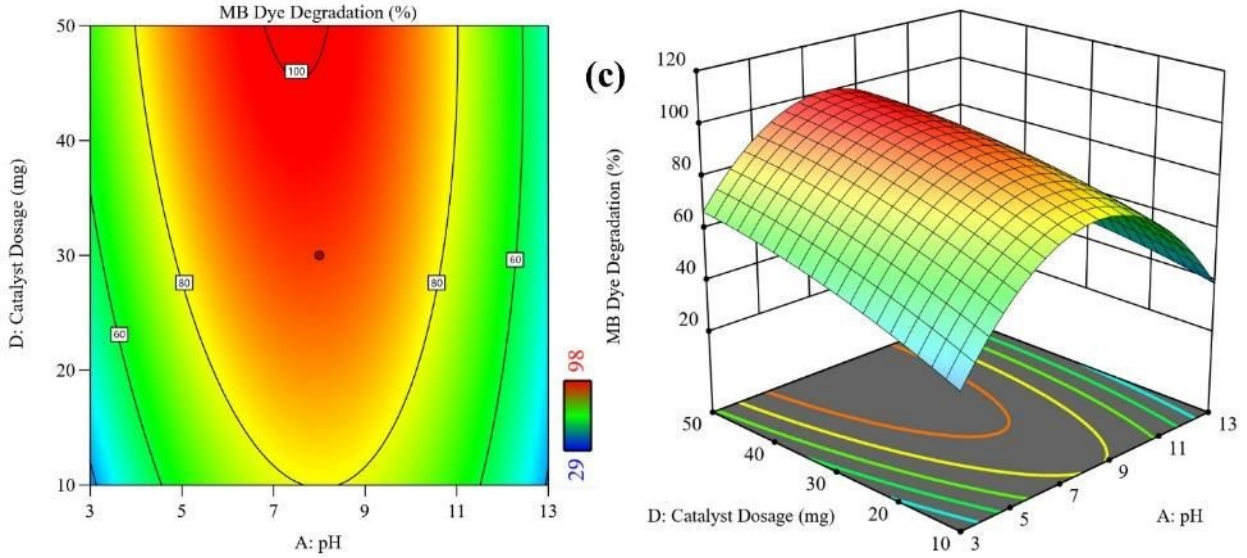

382

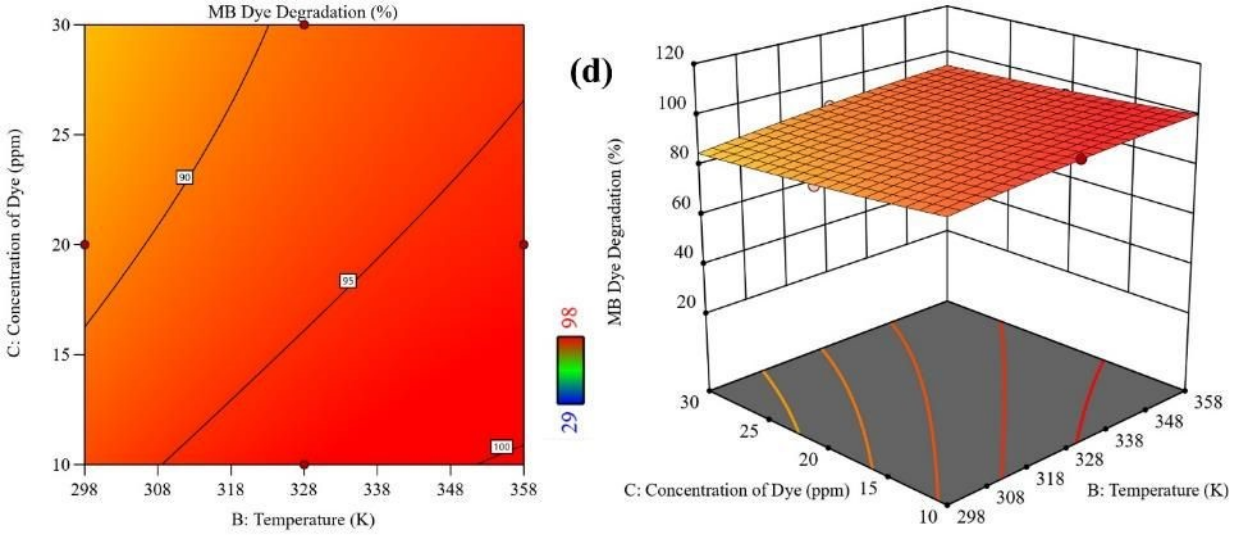

383

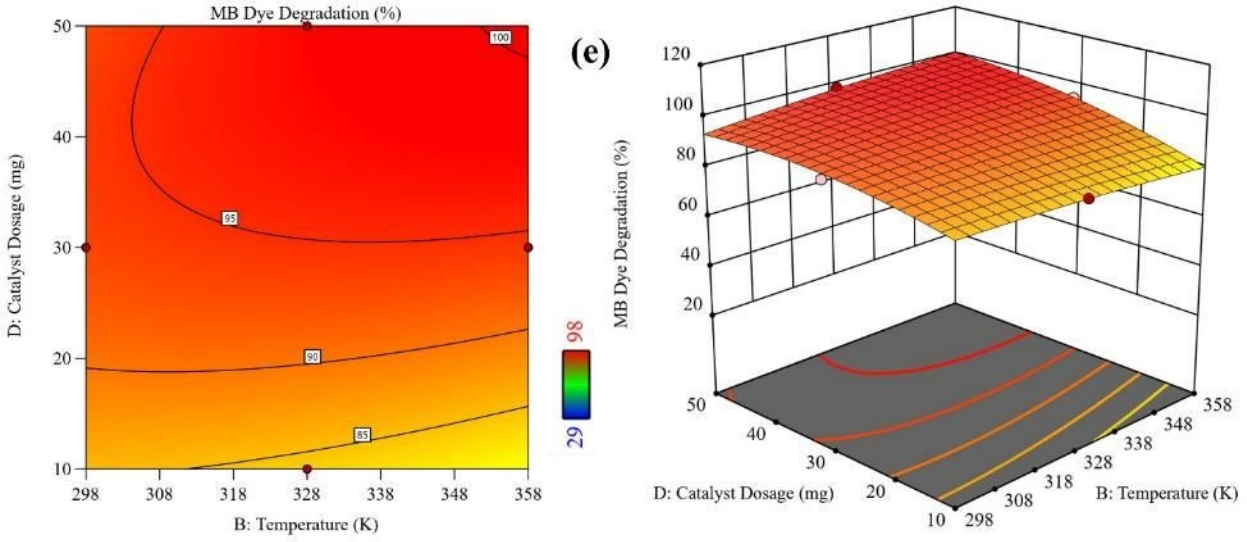

384

View Article Online
DOI: 10.1039/D5NA01159K

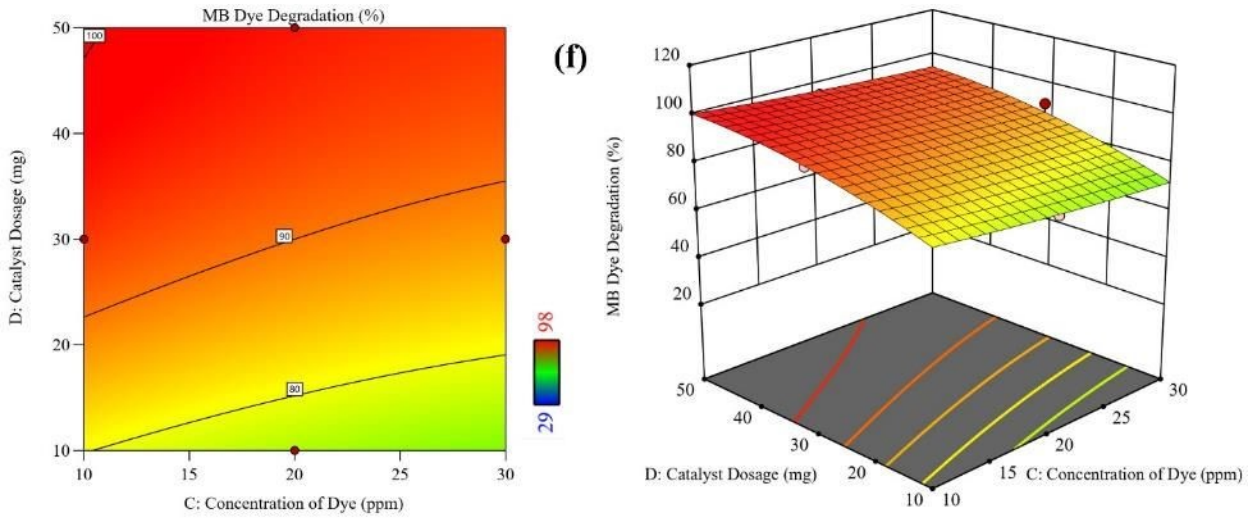

Figure 6. Two-dimensional contour and three-dimensional response plots of effects parameters: **(a)** pH of medium and temperature (K), **(b)** pH of medium and initial dye concentration (ppm), **(c)** pH of medium and CMFE@CuO NPs dosage (mg), **(d)** Temperature (K) and initial dye concentration (ppm), **(e)** Temperature (K) and CMFE@CuO NPs dosage (mg), and **(f)** Initial dye concentration (ppm) and CMFE@CuO NPs dosage (mg)

Figure 6a shows that at pH 8, increasing temperature enhanced degradation efficiency, and the maximum degradation (98%) was achieved at 328 K, a catalyst dosage of 50 mg, and a dye concentration of 10 ppm. It was also observed that the degradation efficiency could reach 100% at 348 K. Furthermore, the F-values of the independent factors indicate that pH had the most tremendous impact on degradation. Since MB is a redox indicator, a pH change significantly impacts the nanomaterial's surface charge, dye ionic nature, adsorption potential, and band potentials. Its color and λ_{max} (668 nm) are not affected by changes in solution pH. The resonance structures of MB are shown in **Figure S6**. However, a low pH can lead to particle agglomeration due to neutralization of surface charge, which in turn reduces surface area, diminishes dye adsorption, and limits the overall photocatalytic potential. It was observed that at pH > 9, CMFE@CuO NPs began to ionize via hydrolysis, leading to a significant decrease in NP

View Article Online
DOI: 10.1039/D5NA01159K

concentration and a subsequent decline in photocatalytic efficiency. However, degradation efficacy significantly rose at pH around 7 due to optimal dye adsorption but dropped again at lower pH as H^+ ions scavenged the ^{-}OH and $^{\bullet}OH$ radicals. Thus, effective control over pH is vital for efficient degradation of organic pollutants.

In addition to pH, catalyst dosage considerably affects degradation efficiency as evidenced by the F-value. It was shown that increasing the catalyst dose considerably enhanced the degradation efficiency by supplying more reactive sites. Yet, large dosages can limit the efficiency since particles agglomerate and cause turbidity in suspension, which in turn blocks the efficient light penetration. Thus, the greatest photocatalytic efficacy was attained at pH 8 with a catalyst dosage of ~50 mg, as shown in **Figure 6c**.

Alongside pH and catalyst dosage, the initial dye concentration was found as a critical factor impacting degradation efficiency. As demonstrated in **Figures 6b** and **6f**, maximal degradation took place at the lowest dye concentration at pH 8 with a catalyst dosage of 50 mg. Increasing dye concentration enhanced competition for active sites on the catalyst surface, limiting degradation efficiency over the 120-minute reaction period due to limited number of reactive sites. At extremely high dye concentrations, degradation efficiency dropped further due to lower light penetration, hence inhibiting photocatalytic activity.

Moreover, temperature showed a relatively small influence on dye degradation, as illustrated in **Figures 6(d-e)**. ANOVA analysis indicated that increasing temperature slightly enhanced degradation rates by increasing the kinetic energy of dye molecules, although its overall contribution to efficiency remained limited.

The cumulative effect of variables on the MB degradation (%) was better elaborated by the 3D response plots. The interactive effect of pH and temperature (Figure 6a) demonstrated that the MB

View Article Online
DOI: 10.1039/D5NA01159K

degradation (%) can be enhanced with an increase in temperature and pH, reaching a maximum value (99.9 %) at pH 8 and 358 K. At the highest temperature, the increase of pH above 8 decreased the degradation efficiency due to ionization of CMFE@CuO NPs and reduction of ROS in the system.

The interactive effect of initial concentration of dye and pH (Figure 6b) showed the increase of MB degradation (%) with a decrease of dye concentration up to 10 ppm and increase of pH up to 8. Maximum degradation (98%) was observed at pH 8 and dye concentration of 10 ppm at 328 K. Similarly, the interactive plots of pH and catalyst dose (Figure 6c), temperature and initial dye concentration (Figure 6d), catalyst dose and temperature (Figure 6e), and catalyst dose and initial dye concentration (Figure 6f) showed that the MB degradation (%) was increased with increase of catalyst dosage (maximum at 50 mg), temperature (up to 358 K), and pH (up to 8), while decreased at high concentration of dye (above 10 ppm).

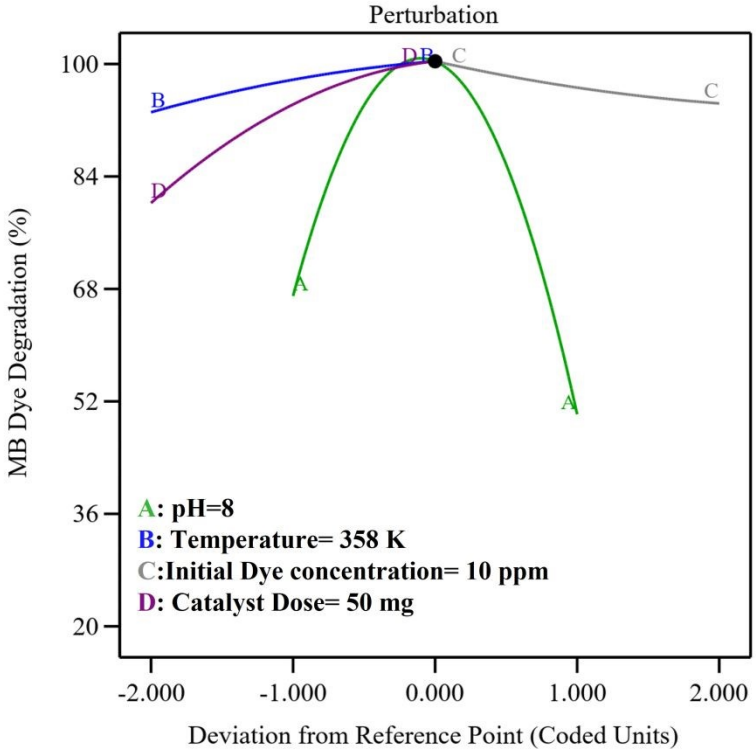

Figure 7. Perturbation plot of interfering reaction parameters

View Article Online
DOI: 10.1039/D5NA01159K

Figure 7 illustrated the collective outcome of reaction conditions on MB degradation. The perturbation graph demonstrates that degradation (%) was decreased when pH goes away from the ideal pH 8 possibly from changes in NPs surface charge or ionization. At a higher catalyst dose accompanied by a high temperature enhanced the degradation efficiency (%) by providing more active sites and kinetic energy to molecules to overcome the energy barrier, respectively. However, dye degradation (%) was increased with decreasing dye concentration (ppm) due to the greater light penetration into the cell.

The optimization of reaction parameters indicated that the maximum degradation efficiency (99.9 %) achieved at relatively milder conditions (50 mg catalyst, 10 ppm dye, pH 8, and temperature of 358 K), suitable for commercial applications of synthesized CMFE@CuO NPs. pH 8 indicated that the process operates effectively under near-neutral to slightly alkaline conditions, minimizing the need for extensive pH adjustment in real wastewater systems. The optimized dye concentration of 10 ppm, characteristic of diluted industrial effluents, indicated the process's potential for wastewater treatment. A moderate catalyst dose of 50 mg emphasized cost-effectiveness by minimizing material use and secondary waste. The optimal operational temperature of 358 K implied that the process can be conducted at manageable temperatures, achievable in practical situations without significant energy requirements. These optimized parameters collectively affirm the feasibility, economic viability, and environmental compatibility of the catalytic system for application in real-world wastewater management.

Degradation kinetics were evaluated using **Equation 1** at 15-minute intervals for a total duration of 120 minutes utilizing the absorbance spectra of MB illustrated in **Figure 8a**. The percentage degradation of MB increased slightly with increasing reaction medium temperature, reaching a

View Article Online
DOI: 10.1039/D5NA01159K

maximum of 99.9% at 358 K. The kinetics models (zero-order, pseudo-first-order, and pseudo-second-order) were applied to examine the degradation kinetics using **Equations 7-9**.

$$C_t = C_0 - k_0 t \quad (7)$$

$$\ln \frac{C_o}{C_t} = k_1 t \quad (8)$$

$$\frac{1}{C_t} = \frac{1}{C_0} + k_2 t \quad (9)$$

C_0 and C_t are the initial dye concentration and dye concentration at any time t, respectively, and k_0, k_1, and k_2 are dye degradation rate constants for zero, 1st, and second-order kinetic models, respectively. The dye degradation data were fitted to zero-, first-, and second-order reaction kinetic models. The fitting of data to zero-, first- and second-order kinetic models is presented in **Figure S7(a-c)**. The values of regression coefficients (R^2) for zero-, first- and second-order reaction kinetic models were found to be 0.871, 0.990, and 0.837, respectively. The results indicate that the dye degradation process obeyed the first-order kinetics. Therefore, the values of rate constants at different temperatures were determined by using **Equation 8**. The slopes of the degradation plots (**Figure 8b**) give the degradation rate constants (k) values of 2.21 x 10^{-2} min^{-1}, 2.71 x 10^{-2} min^{-1}, 3.24 x 10^{-2} min^{-1}, 3.67 x 10^{-2} min^{-1} and 4.44 x 10^{-2} min^{-1} at 298 K, 313 K, 328 K, 343 K, and 358 K. When compared with previously documented catalysts as depicted in **Table S2**, the currently prepared CuO NPs demonstrated superior efficacy against the degradation of MB.

View Article Online
DOI: 10.1039/D5NA01159K

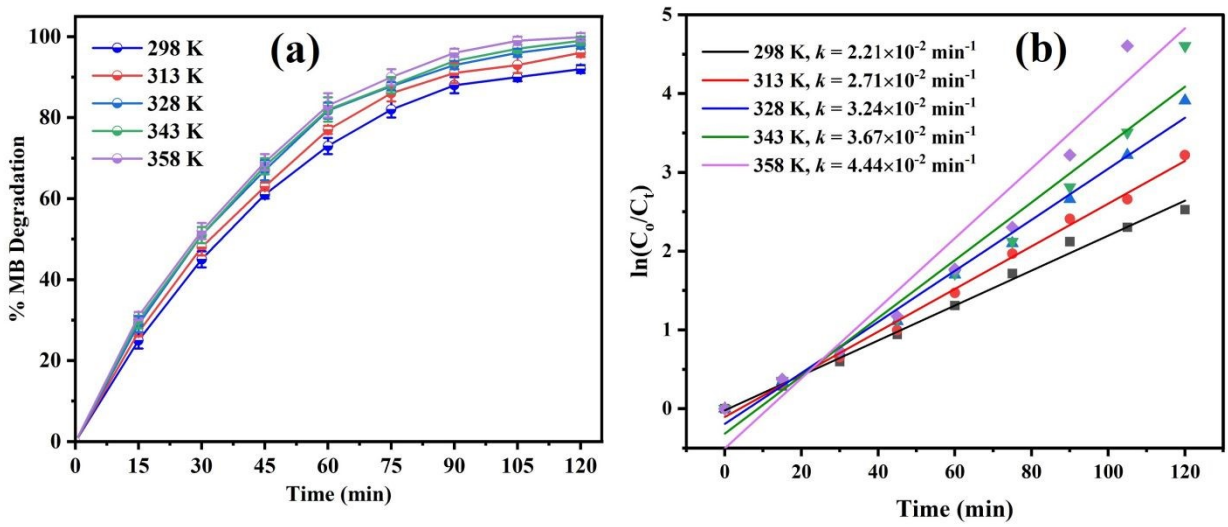

Figure 8. (a) Time-dependent degradation of MB**; (b)** Effect of temperature on rate constant values

3.8.Effect of radical scavengers and proposed mechanism

ROS play a central role in the rapid degradation of organic pollutants [54]. To elucidate the photocatalytic degradation mechanism and identify the dominant reactive species, batch-wise radical scavenging experiments were performed. P-Benzoquinone (p-BQ), isopropanol (IPA), disodium ethylenediaminetetraacetate (Na_2EDTA), and L-ascorbic acid (L-AA) were employed as selective scavengers for $O_2•^-$, •OH, h^+, and H_2O_2, respectively [55]. Each experiment was performed at optimal conditions (50 mg/20 mL catalysts dose, pH 8, 10-ppm dye solution) with the addition of 10 mL of a 0.2 mM scavenger solution. Degradation efficiency (%) was calculated using the above-mentioned procedure.

View Article Online
DOI: 10.1039/D5NA01159K

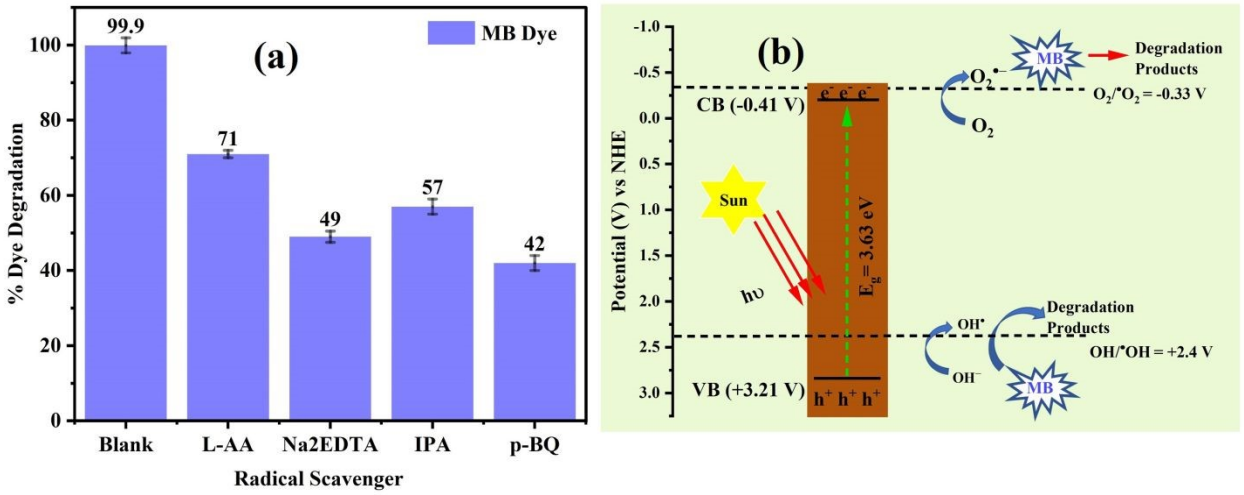

Figure 9. (a) Degradation of MB in presence of radical scavenegrs and **(b)** Band edge potentials of CMFE@CuO NPs for generation of ROS in presence of sunlight to degrade dye

Radical scavenging assays showed the decomposition efficiency diminished in presence of all scavengers, as shown in **Figure 9a**. This result showed that all ROS were produced in the solution as a result of sunlight exposure. The degradation phenomena were most significantly prevented in the presence of p-BQ, followed by Na_2EDTA and IPA. This implies that h^+ and OH• had secondary roles in the degradation process, but $O_2^{-\bullet}$ was an active participant.

The Butler-Ginley equations (**S3 of supplementary information**) were used to calculate the edge potentials of VB and CB in order to obtain a thorough grasp of electron transport and degradation mechanisms [56].

The values of E_{CB} and E_{VB} were determined to be -0.41 V and +3.21 V, respectively as illustrated in **Figure 9b**. The viable reduction and oxidation potentials enable easy formation of reactive oxygen species (ROS), including $O_2^{-\bullet}$, h^+, and $OH^{\bullet}$, at the surface of catalyst in solution, as depicted **in Figure 9b**.

View Article Online
DOI: 10.1039/D5NA01159K

The small potential difference for electron transfer to molecular oxygen facilitated the production of oxide ion radicals, highlighting their role as principal species involved in degradation reactions.

The catalytic decomposition pathway of MB dye was postulated by studying the influence of radical scavengers on the process, as presented in **S3 of supplementary material**. It was hypothesized under sunlight irradiation, the catalyst's valence electrons would be stimulated to the conduction band, resulting in the formation of e^- and h^+ in CB and VB. Oxide ion radicals were formed by reaction of O_2 with e- in CB and OH• radicals were formed by reaction of h^+ with water. Dye degradation involves the production of a variety of secondary radicals in the mixture as a result of secondary reactions.

3.9. TOC analysis results

The estimated TOC values showed that dye mineralization was a sluggish phenomenon compared to color disappearance, with 81% mineralization of MB dye under sunlight illumination for 4 h as shown in **Figure 10a**. This slow rate is attributed to the gradual breakdown of stable components and by-products formed during photodegradation.

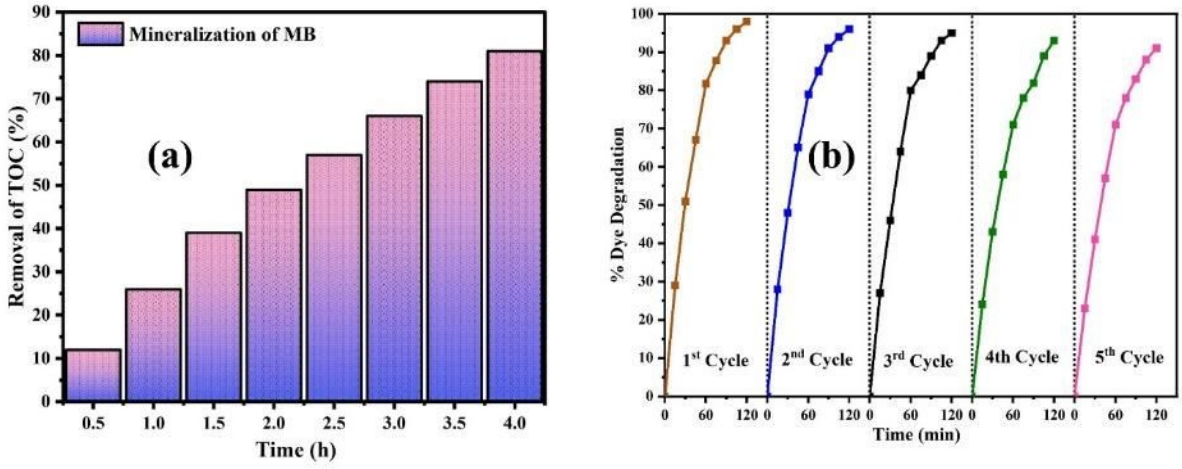

View Article Online
DOI: 10.1039/D5NA01159K

Figure 10. (a) Percentage mineralization of MB at different time intervals during photocatalytic degradation and **(b)** reusability performance of CMFE@CuO NPs over successive degradation cycles.

3.10. Reusability analysis of the photocatalyst

Reusability of the photocatalyst was tested for five consecutive cycles of MB dye degradation using the previously reported method [21, 57]. In short, the catalyst, namely the CMFE@CuO NPs, was extracted by spinning the solution at 3000 rpm for 30 minutes. The solid catalyst was dried for four hours at 80 ºC and then rinsed three times with distilled water to make it suitable for reuse. **Figure 11b** shows the catalyst's reusability with minimal activity loss. After several repeated cycles, the catalyst retained most of its activity with only 7% drop showing its durability and effectiveness for repeated usage. The mechanical stability of the catalyst was also assessed by recording the comparative PXRD and FTIR spectra of the catalyst after five times usage as depicted in Figure 11(a-b). After five consecutive uses, the PXRD spectrum of regenerated CMFE@CuO NPs (Figure 11a) retained all its distinctive peaks, suggesting that the crystalline structure of catalyst remained intact. However, a slight increase in crystallite size was observed from 16.9 nm to 18.9 nm after regeneration. The values of the crystallite parameters depicted in Table 4 indicate the catalyst's high mechanical stability for practical applications. Similarly, the comparison of FTIR spectra (**Figure 11b**) showed the chemical stability of the catalyst as all the functional groups' peaks were retained in the regenerated catalyst. The only hydroxyl peak (-OH) around 3300-3600 cm^{-1} was observed to become more prominent in the regenerated catalyst, which can be due to the adsorbed moisture on the surface of catalyst. Hence, the catalyst presented appears to be suitable for multiple uses in wastewater treatment after proper activation.

View Article Online
DOI: 10.1039/D5NA01159K

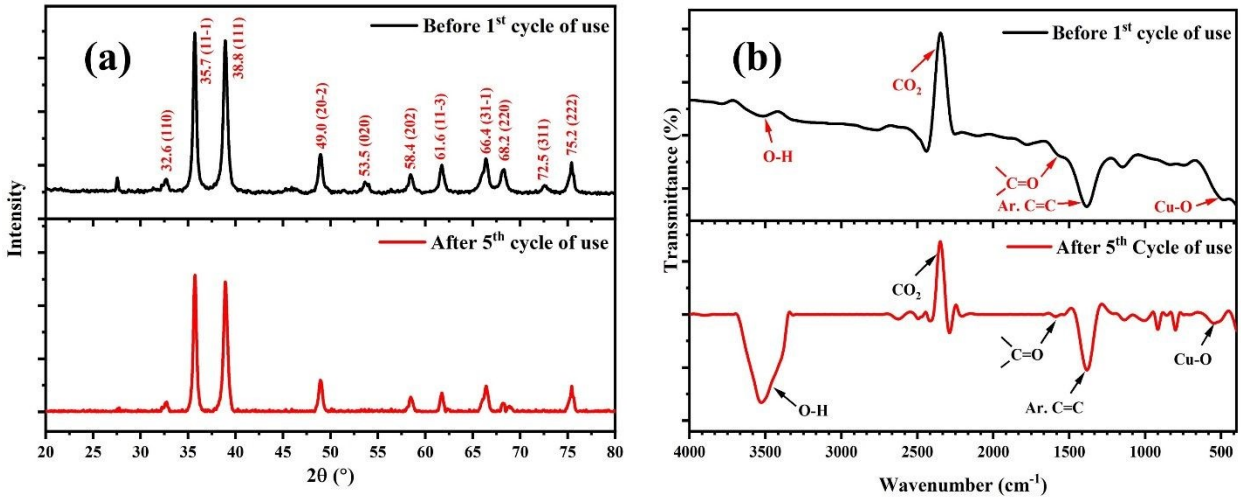

Figure 11. (a) Comparative PXRD spectra of freshly prepared CMFE@CuO NPs and after five times usage, **(b)** Comparative FTIR spectra of freshly prepared CMFE@CuO NPs and after five times usage

Table 4. Crystal parameters of CMFE@CuO NPs after 5th cycle of use

Sample	Average crystallite size 'D' (nm)	Dislocation density δ×10^{-3} (nm^{-2})	Micro strain ε×10^{-3}	Degree of Crystallinity (%)
CMFE@CuO NPs	18.9	2.7	0.59	95.2

The leaching of heavy metal ions, like Cu^{2+}, into freshwater reservoirs may affect the quality of aquatic animals' lives. An elevated level of Cu^{2+} in the freshwater may induce oxidative stress in aquatic animals. Therefore, the leaching of Cu^{2+} ions from the CMFE@CuO NPs catalyst's surface was quantified by atomic absorption spectroscopy (AAS) [58]. For this purpose, after each degradation cycle, the reaction mixture was centrifuged, and the filtrate was analyzed using Graphite furnace atomic absorption spectrometer (AA-6300, Shimadzu Japan). The results

View Article Online
DOI: 10.1039/D5NA01159K

indicated that the concentration of leached Cu^{2+} ions was just 8 ppm after the 5th cycle of use, demonstrating minimal dissolution of the catalyst (only 0.32 %).

This low level of copper leaching (below 1%) highlighted the highly stable and reusable nature of greenly synthesized CMFE@CuO NPs, and supported the reusability analysis results and post-usage PXRD and FTIR analysis of the catalyst. The low leaching level of the catalyst also emphasized that the MB dye degradation reaction was predominantly driven by heterogeneous catalysis rather than homogeneous contributions from dissolved Cu^{2+} ions. All these analyses results highlighted the consistent degradation efficiency of reported greenly synthesized CMFE@CuO NPs over multiple cycles and their suitability for repeated wastewater treatment applications.

3.11. Environmental implications and safe disposal strategies of CMFE@CuO NPs

The presence of excessive leached Cu^{2+} ions in the treated water may affect aquatic animals if the effluent is released directly into freshwater bodies. Although the reported catalyst has shown minimal Cu^{2+} leaching (0.32%) after several cycles and can be used to treat wastewater, the recovery of the leached Cu^{2+} ions is still essential for sustainable application. To minimize the environmental implications and for the safe disposal of catalyst, the following steps must be taken.

1. The CMFE@CuO NPs must be efficiently recovered after each cycle by centrifugation to minimize the environmental discharge.
2. The treated effluent should be monitored to ensure that residual copper levels comply with environmental regulations before disposal. The excess Cu^{2+} should be removed by additional operations such as adsorption, ion exchange, or precipitation [59].

View Article Online
DOI: 10.1039/D5NA01159K

3. If the catalyst becomes inactivated after several uses, it should be collected and either regenerated for reuse or disposed of according to hazardous waste management guidelines.

3.12. Antibacterial and antioxidant activities of CMFE@CuO NPs

The disc diffusion assay assesses the antibacterial potential of CMFE and CMFE@CuO NPs against *S. aureus, B. subtilis, E. coli,* and *P. aeruginosa* bacterial strains. CMFE exhibits strong antibacterial potential [20]. Antimicrobial testing was conducted on samples to ascertain the synergistic effect of NPs mixed with bioactive capping agents. Encapsulating NPs with phytochemical compounds exerted a synergistic effect, markedly enhancing their antibacterial efficacy. **Figure 12a** illustrates the antibacterial efficacy of CMFE in comparison to CMFE@CuO NPs.

View Article Online
DOI: 10.1039/D5NA01159K

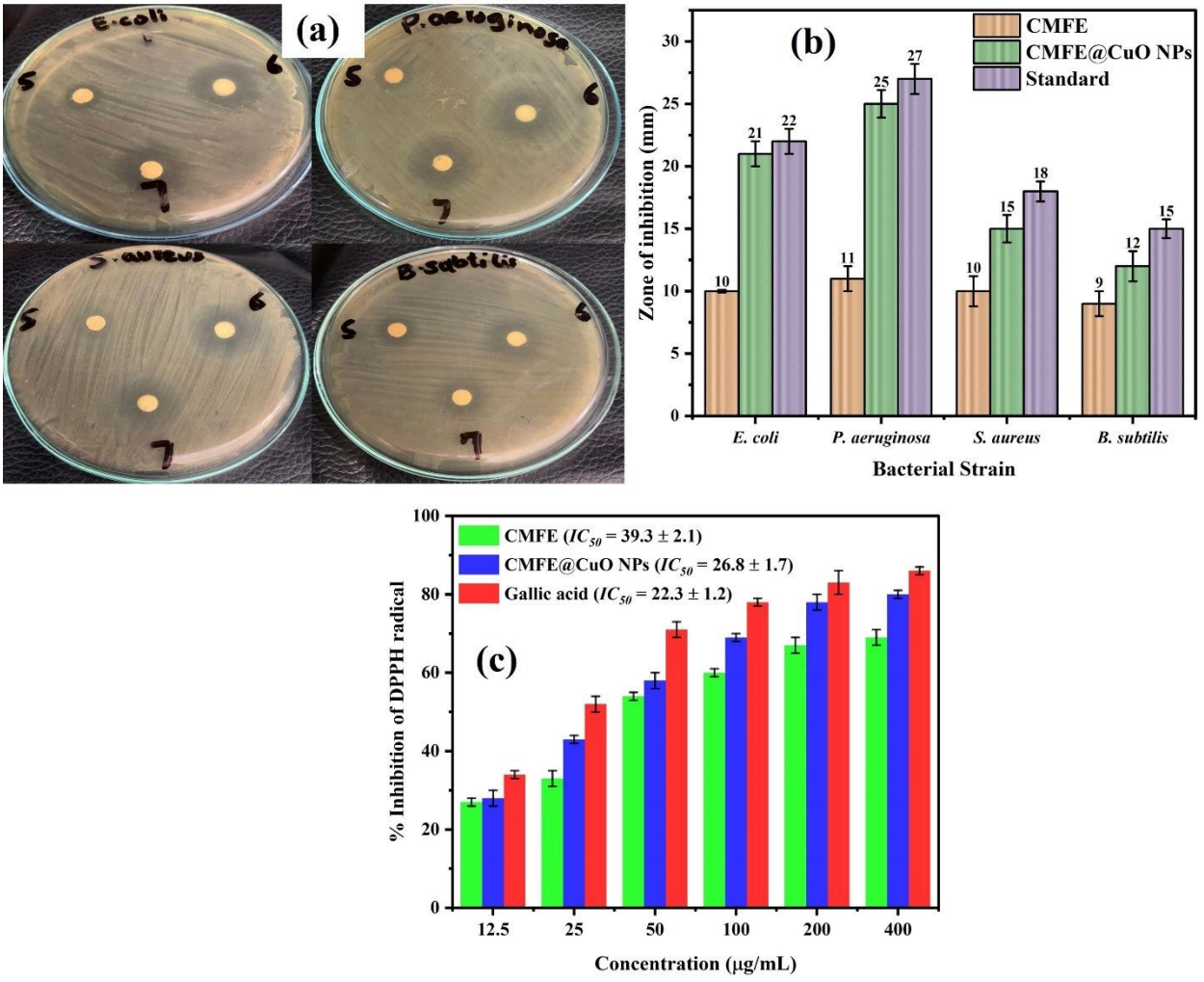

Figure 12. (a) Images of disc diffusion assay showing zone of inhibition of CMFE (5), positive control (6) and CMFE@CuO NPs (7) against bacterial strains, **(b)** Zones of inhibition exhibited by CMFE, CMFE@CuO NPs, and erythromycin (standard) against different bacterial strains, and, **(c)** Antioxidant activity of CMFE, CMFE@CuO NPs, and gallic acid (standard).

The zone of inhibition results demonstrated that CMFE@CuO NPs exhibited greater potency in inhibiting bacterial growth than CMFE (**Figure 12b**). CMFE@CuO NPs showed increased sensitivity to gram-negative bacterial strains, as evidenced by large inhibition zones against *E. coli* (21±1.0 mm) and *P. aeruginosa* (25±1.1 mm) as compared to gram-positive bacteria, i.e., *S. aureus* (15±1.1 mm) and *B. subtilis* (12±1.2 mm). The activity of CMFE@CuO NPs against gram-

View Article Online
DOI: 10.1039/D5NA01159K

negative bacteria was found in close agreement with the standard drug, erythromycin. The MIC values of the CMFE, CMFE@CuO NPs, and the standard are depicted in Table 5.

Table 5. MIC values of CMFE and CMFE@CuO NPs against bacterial strains

Sample	MIC Value (µg/mL)			
	E. coli	***P. aeruginosa***	***S. aureus***	***B. subtilis***
CMFE	315±4.5	289±3.2	322±2.7	342±5.2
CMFE@CuO NPs	118±2.3	103±4.1	182±3.5	217±3.3

The precise mechanism of action remained unidentified; however, numerous studies indicate that NPs exert their effects by infiltrating bacterial cells, generating ROS both intracellularly and extracellularly, producing metal ions within the cell, inactivating enzyme active sites, and irreversibly binding to genetic material. All these interactions culminate in cell death, either by the rupture of the cell wall and subsequent plasma discharge or by impairing the proper functioning of the cells. The exceptional efficacy of CMFE@CuO NPs against Gram-negative bacteria was attributed to differences in the bacterial cell membranes [21, 60, 61]. Gram-negative bacteria have thin cell walls, which make it possible for CMFE@CuO NPs to enter and disrupt cellular functions, increasing antibacterial activity.

Gallic acid was used as a standard because of its well-known capacity to neutralize DPPH radicals by hydrogen donation. The DPPH radical scavenging test was used to assess the antioxidant capability of the synthesized samples. The presence of hydroxyl groups, which are well known for their potent antioxidant properties, is responsible for this action. The evaluation of the antioxidant ability of CMFE and CMFE@CuO NPs was further supported by the discovery of –OH functional groups in their FTIR spectra of all samples.

View Article Online
DOI: 10.1039/D5NA01159K

As shown in **Figure 12c**, the DPPH assay findings showed an increase in antioxidant activity for CMFE, CMFE@CuO NPs, and gallic acid that was concentration-dependent. The CMFE@CuO NPs outperformed the standard in terms of antioxidant efficacy at higher doses (400 µg/mL). The quantity of hydroxyl-rich phytoconstituents covering the surface of the NPs is responsible for this increased activity. This pattern was further supported by the IC_{50} values, which showed that CMFE@CuO NPs had a higher radical scavenging efficiency (IC_{50} = 26.8 ± 1.7 µg/mL) than CMFE (IC_{50} = 39.3 ± 2.1 µg/mL). Furthermore, the IC_{50} value of CMFE@CuO NPs was similar to that of gallic acid (22.3 ± 1.2 µg/mL), highlighting their strong antioxidant potential.

For further validation of the importance of the currently synthesized CMFE@CuO NPs, a comparison of the current work has been depicted in the comparison table (Table 6). The comparison table clearly demonstrated the highly bioactive nature of the synthesized material to inhibit bacterial growth and act as an antioxidant for wastewater treatment.

Table 6. Comparison table of antioxidant Potential of greenly synthesized CuO NPs

Material	Extract	Antioxidant activity by DPPH assay (IC_{50} (µg/mL))	Antibacterial activity (Strain (ZOI))	Reference
CuO NPs	*Solanum nigrum leaf*	189.12	*E. coli* (12 ± 0.1 nm), *B. subtilis* (11 ± 0.3 nm), *S. saprophyticus* (10 ± 0.2 nm) and *P. aeruginosa* (8 ± 0.5 nm)	62
CuO NPs	*Tribulus terrestris* L	51.53	*S. aureus* (17 mm) and *E. coli* (18 mm)	63
CuO NPs	*Ligustrum lucidum*	63.35	----	64
CuO NPs	*Vernonia amygdalina*	----	*E. coli* (12 mm), *P. aeruginosa* (12 mm), and *E. aerogenes (15 mm)*	65
CuO NPs	*Suaeda maritima* (L.) Dumort	28.05	*B. subtilis (17.1 mm), S. aureus (16.5 mm), E. coli*	66

View Article Online
DOI: 10.1039/D5NA01159K

			(14.3 mm), P. aeruginosa (15.8 mm)	
CuO NPs	Fruit waste	----	*E. coli* (29.0 ± 2.3 mm) and *S. aureus (*26.0 ± 1.1 mm)	[67]
CMFE@CuO NPs	*C. macrocarpa* fruit	26.8±1.7	*E. coli* (21±1.0 mm) and *P. aeruginosa* (25±1.1 mm), *S. aureus* (15±1.1 mm) and *B. subtilis* (12±1.2 mm)	Current Work

Although the greenly synthesized CMFE@CuO NPs have appreciable antimicrobial and antioxidant potential, but the in vivo use of this material is not recommended due to cytotoxicity concerns. However, the results have indicated that this material can be effectively used to purify the wastewater from wastewater-borne microbes and can be used in creams and ointments for external use only.

4. Conclusion

The biogenic synthesis of CuO NPs based on natal plum aqueous extract is presented in this work. With an average particle size of 71 nm and a crystallite size of 16.9 nm, CMFE@CuO NPs have demonstrated a broad bandgap of 3.63 eV, making them appropriate for the production of charge carriers under sunlight on surface of catalyst. CMFE@CuO NPs demonstrated outstanding photodegradation of MB (99.9%) at pH 8, 50 mg catalyst dosage, and 10 ppm dye concentration at 358 K following reaction parameter optimization using the RSM/BBD model. $O_2^{-\bullet}$ showed the primary contribution towards the degradation process, followed by h^+ and $OH^\bullet$ radicals, according to radical scavenging assays. These results were found concordant with the band edge potentials of CMFE@CuO NPs measure to evaluate the generation of major ROS produced. Regeneration studies of the catalyst showed a mere 7% decline in the catalyst's efficiency even after being used five times. CMFE@CuO NPs were also found to be effective antibacterial agents to inhibit the

View Article Online
DOI: 10.1039/D5NA01159K

growth of gram-negative bacteria (*E. coli* (21±1 mm) and *P. aeruginosa* (25±1.1 mm)) as compared to gram-positive bacteria (*S. aureus* (15±1.1 mm) and *B. subtilis* (12±1.2 mm)).In addition, CMFE@CuO NPs have also shown high antioxidant potential (IC_{50} = 26.8±1.7 µg/mL), rivaling that of standard gallic acid (IC_{50} = 22.3±1.2 µg/mL), thereby emphasizing their remarkable potential for industrial wastewater remediation.

CRediT author statement

A. B. Siddique: Methodology, Investigation, Writing –original draft, Writing – review & editing**.** **Y. Zaman** & **A. Abbas**: Data Curation, Writing – review & editing. **M. F.U. Rehman & M. Sher**: Writing review & editing. **U. Nishan & Ibrahim A. Shaaban**: Resources, & Writing – review & editing.

Acknowledgement

The authors extend their appreciation to the Deanship of Research and Graduate Studies at King Khalid University, Saudi Arabia, through Large Research Project under grant number RGP-2/695/46.

Funding

No specific funding was received for this project.

Competing Interests

The authors have no known financial or non-financial interests to disclose.

Availability of data and materials

All evaluated data is available in the manuscript. Additional information/data can be provided upon reasonable request.

References

View Article Online
DOI: 10.1039/D5NA01159K

1. W. U. Khan, S. Ahmed, Y. Dhoble and S. Madhav, *Journal of the Indian Chemical Society*, 2023, **100**, 100829.
2. M. Chahar, S. Khaturia, H. L. Singh, V. S. Solanki, N. Agarwal, D. K. Sahoo, V. K. Yadav and A. Patel, *Frontiers in Environmental Science*, 2023, **11**, 1226101.
3. V. Selvaraj, T. S. Karthika, C. Mansiya and M. Alagar, *Journal of molecular structure*, 2021, **1224**, 129195.
4. Y. Zaman, M. Z. Ishaque, S. Ajmal, M. Shahzad, A. B. Siddique, M. U. Hameed, H. Kanwal, R. J. Ramalingam, M. Selvaraj and G. Yasin, *Inorganic Chemistry Communications*, 2023, **150**, 110523.
5. J. W. Harvey and A. S. Keitt, *British journal of haematology*, 1983, **54**, 29-41.
6. I. Khan, K. Saeed, I. Zekker, B. Zhang, A. H. Hendi, A. Ahmad, S. Ahmad, N. Zada, H. Ahmad and L. A. Shah, *Water*, 2022, **14**, 242.
7. K.-T. Chung, *Journal of Environmental Science and Health, Part C*, 2016, **34**, 233-261.
8. S. M. Shalaby, F. F. Madkour, H. Y. El-Kassas, A. A. Mohamed and A. M. Elgarahy, *International Journal of Phytoremediation*, 2022, **24**, 902-918.
9. , !!! INVALID CITATION !!! 9-12.
10. P. Shandilya, P. Raizada and P. Singh, *Water Pollution and Remediation: Photocatalysis*, 2021, 119-146.
11. M. Z. Ishaque, Y. Zaman, Y. Yousaf, M. Shahzad, A. B. Siddique, H. Zaman, S. Ali and N. Ali, *Water, Air, & Soil Pollution*, 2024, **235**, 43.
12. P. Koteeswari, S. Sagadevan, I. Fatimah, A. K. Sibhatu, S. I. Abd Razak, E. Leonard and T. Soga, *Inorganic Chemistry Communications*, 2022, **144**, 109851.

View Article Online
DOI: 10.1039/D5NA01159K

13. K. Selvam, G. Albasher, O. Alamri, C. Sudhakar, T. Selvankumar, S. Vijayalakshmi and L. Vennila, *Environ Res*, 2022, **211**, 113046.

14. A. Atri, M. Echabaane, A. Bouzidi, I. Harabi, B. M. Soucase and R. B. Chaâbane, *Heliyon*, 2023, **9**.

15. E. Arulkumar, R. K. Manivannan, G. Dhamodaran and R. Krishnan, *Journal of Sol-Gel Science and Technology*, 2025, 1-33.

16. H. Kumar, K. Bhardwaj, D. S. Dhanjal, E. Nepovimova, F. Şen, H. Regassa, R. Singh, R. Verma, V. Kumar and D. Kumar, *International journal of molecular sciences*, 2020, **21**, 8458.

17. S. Suresh, S. Vennila, J. Anita Lett, I. Fatimah, F. Mohammad, H. A. Al-Lohedan, S. F. Alshahateet, M. Motalib Hossain and M. Rafie Johan, *Inorganic and Nano-Metal Chemistry*, 2022, **52**, 173-180.

18. J. O. Adeyemi, A. O. Oriola, D. C. Onwudiwe and A. O. Oyedeji, *Biomolecules*, 2022, **12**, 627.

19. Y. Yang, J. Liu, J. Cao, Z. Zhou and X. Zhang, *Journal of Materials Chemistry C*, 2019, **7**, 578-585.

20. F. Seke, V. E. Manhivi, T. Shoko, R. M. Slabbert, Y. Sultanbawa and D. Sivakumar, *Foods*, 2021, **10**, 1420.

21. A. B. Siddique, M. A. Shaheen, A. Abbas, Y. Zaman, M. A. Bratty, A. Najmi, A. Hanbashi, M. Mustaqeem, H. A. Alhazmi and Z. ur Rehman, *Heliyon*, 2024, **10**, e40679.

22. A. B. Siddique, M. A. Shaheen, A. Abbas, Y. Zaman, H. M. Amin, M. M. Alam, N. K. Alharbi, F. Alshehri, A. Shami and F. A. Al-Joufi, *International Journal of Environmental Analytical Chemistry*, 2025, 1-23.

View Article Online
DOI: 10.1039/D5NA01159K

23. A. B. Siddique, M. A. Shaheen, A. Abbas, Y. Zaman, M. U. Rasheed, A. Karim, M. Mustaqeem, M. M. Alam and A. S. Alahmari, *Water, Air, & Soil Pollution*, 2025, **236**, 1-22.

24. A. B. Siddique, M. A. Shaheen, A. Abbas, Y. Zaman, M. Z. Ishaque, A. Shami, M. Aslam, K. M. Alsyaad and A. Ali, *Journal of Molecular Structure*, 2025, **1331**, 141566.

25. A. B. Siddique, M. A. Shaheen, S. Shafeeq, A. Abbas, Y. Zaman, M. Z. Ishaque and M. Aslam, *Materials Advances*, 2025, **6**, 1330-1344.

26. A. B. Siddique, M. A. Shaheen, A. Abbas, S. Akhtar, M. Shahzad, A. Ali, N. Ahmad, H. A. Abuelizz and R. Al-Salahi, *Fuel*, 2026, **406**, 137178.

27. A. Zhou, Q. Wu, H. Zhang, J. Liu, C. Wang, D. Chi and H. Zhou, *Journal of Environmental Management*, 2026, **401**, 128837.

28. G. K. Weldegebrieal, H. H. Dube and A. K. Sibhatu, *International Journal of Environmental Analytical Chemistry*, 2023, **103**, 6146-6168.

29. J. Wu, X. Yue, T. Wang, Y. Zhang, Y. Jin and G. Li, *Colloids and Surfaces A: Physicochemical and Engineering Aspects*, 2025, **717**, 136850.

30. Y. Deng, B. Li, H. Zheng, L. Liang, Y. Yang, S. Liu, M. Wang, C. Peng, B. Liu and W. Wang, *Asian Journal of Pharmaceutical Sciences*, 2025, **20**, 101037.

31. Y. Nie, D. Li, Y. Peng, S. Wang, S. Hu, M. Liu, J. Ding and W. Zhou, *International journal of pharmaceutics*, 2020, **585**, 119513.

32. S. Kanwar and S. Vijayavenkataraman, *International Journal of Bioprinting*, 2024, **10**, 4538.

33. X. Wang, K. Sun, J. Dong, Y. Ge, H. Liu, X. Jin, X. Pei, P. Wang, J. Jiang and T. Wang, *Materials Today Bio*, 2025, 102278.

View Article Online
DOI: 10.1039/D5NA01159K

34. H. Ren, Y. Quan, S. Liu and J. Hao, *Ultrasonics Sonochemistry*, 2025, **112**, 107190.

35. A. Waris, M. Din, A. Ali, M. Ali, S. Afridi, A. Baset and A. U. Khan, *Inorganic Chemistry Communications*, 2021, **123**, 108369.

36. S. A. Akintelu, A. S. Folorunso, F. A. Folorunso and A. K. Oyebamiji, *Heliyon*, 2020, **6**.

37. A. B. Siddique, M. A. Shaheen, A. Abbas, Y. Zaman, A. Ali, M. N. ul Hassan and J. Iqbal, *Journal of Environmental Chemical Engineering*, 2024, 112725.

38. N. F. Ibarra-Cervantes, E. Vázquez-Núñez, C. Gómez-Solis, F. Fernández-Luqueño, G. Basurto-Islas, J. Álvarez-Martínez and R. Castro-Beltrán, *Environmental Science and Pollution Research*, 2024, 1-17.

39. M. Niaz, H. Abrar, S. Ashfaq, N. Khan, M. Awais, N. e Baseerat, R. Jadoon, A. Abrar, M. Kashif and K. Ullah, *Phytopharmacology Research Journal*, 2024, **3**, 31-38.

40. A. B. Siddique, D. Amr, A. Abbas, L. Zohra, M. I. Irfan, A. Alhoshani, S. Ashraf and H. M. Amin, *Int J Biol Macromol*, 2024, **256**, 128009.

41. A. Ejaz, Z. Mamtaz, I. Yasmin, M. Shaban, A. B. Siddique, M. I. Irfan, A. Ali, S. Muhammad, M. Y. Sameeh and A. Abbas, *Journal of Molecular Liquids*, 2023, 123622.

42. Y. Zaman, M. Z. Ishaque, K. Waris, M. Shahzad, A. B. Siddique, M. I. Arshad, H. Zaman, H. M. Ali, F. Kanwal and M. Aslam, *Arabian Journal of Chemistry*, 2023, **16**, 105230.

43. H. Saha, A. Dastider, M. J. F. Anik, S. R. Mim, S. Talapatra, U. Das, M. Jamal and M. M. Billah, *Results in Materials*, 2024, **24**, 100614.

44. H. Ahsan, M. Shahid, M. Imran, F. Mahmood, M. H. Siddique, H. M. Ali, M. B. Niazi, S. Hussain, M. Shahbaz and M. Ayyub, *PeerJ*, 2022, **10**, e14358.

45. I. K. Konstantinou and T. A. Albanis, *Applied Catalysis B: Environmental*, 2004, **49**, 1-14.

View Article Online
DOI: 10.1039/D5NA01159K

760 46. W. W. Anku, S. O.-B. Oppong, S. K. Shukla and P. P. Govender, *Acta Chimica Slovenica*,
761 2016, **63**.
762 47. C. Lara-Pérez, E. Leyva, B. Zermeño, I. Osorio, C. Montalvo and E. Moctezuma,
763 *Environmental Earth Sciences*, 2020, **79**, 277.
764 48. Y. Zaman, M. Z. Ishaque, Y. Yousaf, M. Shahzad, A. B. Siddique, M. I. Arshad, M. Sajid,
765 N. Ali and G. Nabi, *Environmental Science and Pollution Research*, 2023, **30**, 95860-
766 95874.
767 49. M. Z. Ishaque, Y. Zaman, M. Shahzad, A. B. Siddique, S. Shahid, M. Akram, H. Kanwal,
768 M. T. Akhtar and S. Hussain, *Water, Air, & Soil Pollution*, 2023, **234**, 252.
769 50. M. S. Ahmad, A. B. Siddique, M. Khalid, A. Ali, M. A. Shaheen, M. N. Tahir, M. Imran,
770 A. Irfan, M. U. Khan and M. W. Paixão, *RSC advances*, 2023, **13**, 9222-9230.
771 51. N. R. Dhineshbabu, V. Rajendran, N. Nithyavathy and R. Vetumperumal, *Applied*
772 *Nanoscience*, 2016, **6**, 933-939.
773 52. A. B. Siddique, S. Ahmad, M. A. Shaheen, A. Ali, M. N. Tahir, L. C. Vieira, S. Muhammad
774 and S. M. Siddeeg, *CrystEngComm*, 2022, **24**, 8237-8247.
775 53. M. Z. Ishaque, Y. Zaman, A. Arif, A. B. Siddique, M. Shahzad, D. Ali, M. Aslam, H.
776 Zaman and M. Faizan, *RSC advances*, 2023, **13**, 30838-30854.
777 54. J. Neto, S. Satyro, E. Saggioro and M. Dezotti, *International Journal of Environmental*
778 *Science and Technology*, 2021, **18**, 163-172.
779 55. D. T. C. Nguyen, H. T. Le, T. T. Nguyen, T. T. T. Nguyen, L. G. Bach, T. D. Nguyen and
780 T. Van Tran, *J Hazard Mater*, 2021, **420**, 126586.
781 56. M. A. Ashraf, C. Li, D. Zhang, L. Zhao and A. Fakhri, *Int J Biol Macromol*, 2021, **169**,
782 436-442.

View Article Online
DOI: 10.1039/D5NA01159K

57. M. A. Ansari, M. Murali, D. Prasad, M. A. Alzohairy, A. Almatroudi, M. N. Alomary, A. C. Udayashankar, S. B. Singh, S. M. M. Asiri and B. S. Ashwini, *Biomolecules*, 2020, **10**, 336.

58. N. A. Kassim, S. Ghazali, F. L. Bohari and N. Abidin, *Materials Today: Proceedings*, 2022, **66**, 3961-3964.

59. Y. Liu, H. Wang, Y. Cui and N. Chen, *International journal of environmental research and public health*, 2023, **20**, 3885.

60. Y. Y. Loo, Y. Rukayadi, M.-A.-R. Nor-Khaizura, C. H. Kuan, B. W. Chieng, M. Nishibuchi and S. Radu, *Frontiers in microbiology*, 2018, **9**, 1555.

61. S. Meghana, P. Kabra, S. Chakraborty and N. Padmavathy, *RSC advances*, 2015, **5**, 12293-12299.

62. A. Muthuvel, M. Jothibas and C. Manoharan, *Nanotechnology for Environmental Engineering*, 2020, **5**, 14.

63. M. Palani, S. Kalaiselvan, J. A. M. Mark, K. Chandran and V. Ekhambaram, *Aspects of Molecular Medicine*, 2024, **4**, 100049.

64. M. C. Ogwuegbu, A. S. Ayangbenro, D. M. Mthiyane, O. O. Babalola and D. C. Onwudiwe, *Materials Research Express*, 2024, **11**, 055010.

65. H. A. Murthy, T. D. Zeleke, K. Tan, S. Ghotekar, M. W. Alam, R. Balachandran, K.-Y. Chan, P. Sanaulla, M. A. Kumar and C. Ravikumar, *Results in Chemistry*, 2021, **3**, 100141.

66. P. Peddi, P. R. Ptsrk, N. U. Rani and S. L. Tulasi, *Journal of Genetic Engineering and Biotechnology*, 2021, **19**, 131.

67. R. Rajamohan, C. J. Raorane, S.-C. Kim and Y. R. Lee, *Materials*, 2022, **16**, 217.

View Article Online
DOI: 10.1039/D5NA01159K

Availability of data and materials

All evaluated data is available in the manuscript. Additional information/data can be provided upon reasonable request.